

Special Section:Years of the Maritime
Continent

Reciprocity in the Indian Ocean: Intraseasonal Oscillation and Ocean Planetary Waves

Adam V. Rydbeck¹ , Tommy G. Jensen¹ , and Maria K. Flatau² ¹U.S. Naval Research Laboratory, Stennis Space Center, MS, USA, ²U.S. Naval Research Laboratory, Monterey, CA, USA**Key Points:**

- Rossby waves in the tropical Indian Ocean increase ocean heat content prior to the intensification of intraseasonal oscillation (ISO) convection
- The increase of ocean heat content is mainly due to ocean dynamics including vertical and meridional advection
- The oceanic Rossby waves link successive atmospheric ISOs

Correspondence to:A. V. Rydbeck,
adam.rydbeck@nrlssc.navy.mil**Citation:**Rydbeck, A. V., Jensen, T. G., & Flatau, M. K. (2021). Reciprocity in the Indian Ocean: Intraseasonal oscillation and ocean planetary waves. *Journal of Geophysical Research: Oceans*, 126, e2021JC017546. <https://doi.org/10.1029/2021JC017546>Received 6 MAY 2021
Accepted 18 AUG 2021

Published 2021. This article is a U.S. Government work and is in the public domain in the USA.

Abstract During the intraseasonal oscillation (ISO) in the tropical Indian Ocean, a recent study observed an interesting relationship between atmospheric convection and ocean heat content anomalies. Ocean heat content anomalies maximize during periods of enhanced convection. Using that study as motivation, the processes responsible for this behavior are further investigated using satellite observations and a state-of-the-art ocean reanalysis. These data show that ocean dynamics linked to first baroclinic mode equatorial Rossby (ER) waves are responsible for the routine synchronization of anomalous ocean heat content and atmospheric convection during the ISO. Using a novel index to identify oceanic ER waves in the Indian Ocean, we observe the following sequence of events indicative of two-way feedbacks between large-scale intraseasonal modes in the atmosphere and ocean: (a) Westerly wind stress associated with the enhanced convective phase of the ISO piles mass in the eastern Indian Ocean forcing a westward oriented pressure gradient along the equator. (b) The easterly wind stress that immediately follows combines with the pressure gradient forcing to generate downwelling ER waves that slowly propagate westward. (c) The waves maximize in the central Indian Ocean where they depress the isotherms and increase the ocean heat content as the next enhanced convective phase of the ISO passes and intensifies. The entire feedback loop transpires over 90 days.

Plain Language Summary A large collection of precipitating clouds and strong winds in the tropical atmosphere, known as the intraseasonal oscillation (ISO), generates planetary waves in the ocean. These waves are only several centimeters tall at the ocean surface, but are capable of transporting large amounts of heat. The planetary waves, also referred to as Rossby waves, travel very slowly and take several months to cross the Indian Ocean from east to west. We observe that these ocean waves are initially generated by the eastward winds within the ISO and subsequently intensified by the westward winds that are in front of the next ISO. The waves increase the amount of warm water in the upper ocean so that when the next ISO arrives, the waves support the development and intensification of clouds and precipitation within the ISO. In short, a portion of the energy from the ISO is stored in the ocean in the form of ocean Rossby waves, which then warm the upper ocean and strengthen the following ISO.

1. Introduction

The Indian Ocean is a unique basin of atmospheric and oceanic intraseasonal variability. In the atmosphere, it is the preferred region for initiation and intensification of the intraseasonal oscillation (ISO) (Kiladis et al., 2014; Madden & Julian, 1971). Intraseasonal wind stress, including that from the ISO, forces counter propagating equatorial Rossby (ER) and Kelvin waves in the ocean. Kelvin waves that reach the eastern boundary reflect as Rossby waves, and Rossby waves that reach the western boundary can reflect as Kelvin waves. Interactions between the wind forced waves and the reflected waves produce a constructive interference that amplifies them on preferred timescales, as demonstrated in many linear models that are consistent with tropical Indian Ocean mooring data (Effy et al., 2020; Fu, 2007; Han, 2005; Han et al., 2001, 2011; Jensen, 1993). Recent linear modeling work showed that most of the westward propagating intraseasonal variability in the ocean results from the first two baroclinic mode ER waves (Nagura & McPhaden, 2012). In the same model, it was shown that the reflection of Rossby wave energy at the western boundary (i.e., Africa) is weak due to the sink of energy by short Rossby waves. As a result, only wind forced waves in the ocean interior and Kelvin waves reflected at the eastern boundary are necessary for intraseasonal resonance in the tropical Indian Ocean.

Several outstanding questions remain regarding interactions of oceanic equatorial waves and the ISO in the Indian Ocean: (a) Do these ocean resonances, previously simulated in linear models, systematically feedback to the atmosphere such that they modify the phase speed or intensity of subsequent ISO events? If so, how? (b) How do successive large-scale alternating wind anomalies associated with the ISO (or other modes of intraseasonal wind stress) preferentially amplify the intrinsic ocean resonance versus dampen it? (c) What large-scale variations in tropical Indian Ocean surface and subsurface conditions occur as a result of the ocean resonance?

The ocean response to intraseasonal forcing may be decomposed into two categories: (a) contemporaneous response and (b) lagged response. In the contemporaneous response category, strong winds and heavy precipitation associated with the active phase of the ISO cool the ocean mixed layer through enhanced surface latent heat fluxes, increased turbulent mixing, and reduced incoming shortwave radiation. During the suppressed phase of the ISO, weak winds, reduced precipitation, and enhanced incoming shortwave radiation warm the ocean mixed layer. As the ISO propagates eastward, SST is maximized just ahead of the convective envelope then rapidly cools as convection advances into the area (DeMott et al., 2015).

Over the last decade, important roles for the second category, the lagged response, have been discovered. These include intraseasonal contributions from large-scale ocean equatorial waves that trail the initial ISO forcing, adding greater complexity to intraseasonal atmosphere-ocean interactions (Azaneu et al., 2021; Rydbeck & Jensen, 2017; Rydbeck et al., 2017; Rydbeck, Jensen, Smith, et al., 2019; Webber et al., 2010; Webber, Matthews, et al., 2012; Webber, Stevens, et al., 2012; West et al., 2018, 2020). These ocean waves arise from the integrated and somewhat lagged ocean response to forcing by ISO wind stress anomalies. Webber et al. (2010) observed that primary ISO events, those with no antecedent atmospheric signals, are often preceded by downwelling ER waves in the ocean. These waves deepen the mixed layer and warm the ocean surface in the western tropical Indian Ocean prior to ISO convective onset.

They hypothesized that these ocean waves are forced by ISO events that occurred several months earlier, creating a positive feedback loop where ISO wind stress drives a downwelling Kelvin wave that reflects at the eastern boundary of the Indian Ocean as ER waves. These waves then arrive in the western Indian Ocean ~90 days later and force a subsequent ISO event by increasing surface latent heat fluxes and converging low-level moisture (Rydbeck & Jensen, 2017) which humidifies the atmospheric boundary layer and prompts convection initiation. The hypothesis has been supported using observations (Rydbeck & Jensen, 2017; Webber, Matthews, et al., 2012; Webber, Stevens, et al., 2012; West et al., 2018, 2020) and a cloud resolving model (Rydbeck, Jensen, & Igel, 2019). These studies suggest that ER waves are partly responsible for the episodic nature of the ISO and may help to explain its broadband behavior, particularly its low-frequency tail. However, this mechanism of ISO initiation is relatively infrequent, occurring once or twice every couple of years (Rydbeck & Jensen, 2017; Webber et al., 2010; Webber, Matthews, et al., 2012; Webber, Stevens, et al., 2012; West et al., 2018, 2020).

While ISO convection onset linked to ocean waves occurs rather intermittently, recent research has indicated a more consistent relationship between ocean waves and the ISO. When averaging strong ISO events from 1994 to 2015, SST anomalies are observed to *cool* during the convectively active phase of the ISO, but anomalous OHC *increases* over the central and western tropical Indian Ocean (Rydbeck, Jensen, Smith, et al., 2019). That is to say, the reservoir of warm water in the upper ocean increases even as surface fluxes and turbulent mixing cool the sea surface. This finding differs from earlier research studies that focused on the initiation of ISO by ER waves. These recently published results, instead, connect the maintenance and intensification of *previously existing* ISO events with ER waves. We hypothesize that the synchronization of intraseasonal atmospheric convection and OHC anomalies in the tropical Indian Ocean, as shown in Rydbeck, Jensen, Smith, et al. (2019), is the result of forcing by first baroclinic mode ER waves in the ocean.

This study is purposed to increase our understanding of the pathways by which planetary waves in the ocean and intraseasonal variability in the atmosphere support a positive feedback loop. While much work has been undertaken to understand the mechanisms by which ocean intraseasonal variability is generated and amplified by the ISO, much less has been done to understand how intraseasonal ocean modes feedback onto the ISO. We extend these previous studies by investigating a new pathway of atmosphere-ocean intraseasonal reciprocation, described by the following series of events. Intraseasonal westerly wind forcing

associated with the ISO accumulates mass in the eastern equatorial Indian Ocean. When the anomalous westerlies switch to easterlies, ER waves are generated and propagated westward by wind stress and pressure gradient forcing. The ER waves amplify under persistent easterly wind stress anomalies associated with the next ISO event. As a result, ER waves are typically strongest in the central Indian Ocean, before ISO easterlies switch to westerlies, and depress the thermocline such that OHC increases. When the enhanced convective phase of the next ISO propagates across the region of anomalously increased OHC, ISO convection is observed to intensify in our study. In other words, the memory of the first ISO event is retained in the form of equatorial waves in the ocean which communicate with the following ISO event via their effect on upper OHC, creating a positive feedback loop. The forcing of ocean equatorial waves by ISO wind stress is well known, however the modulating effect of the ocean on successive ISOs has only recently been explored (Moum et al., 2016). The present study expands on this emerging area of research.

This investigation describes the overall behavior of ER waves as a function of their lifecycle, explains the observed regional dependencies of the leading mode intraseasonal ER waves in the tropical Indian Ocean, and reveals a new feedback loop that supplements the linear modeling research previously mentioned. We are specifically interested in using data from satellites and model reanalysis to examine the ocean planetary wave dynamics hypothesized to control the behavior of intraseasonal OHC anomalies in the tropical Indian Ocean. In order to do this, we develop an objective methodology to detect and catalog intraseasonal ER waves using satellite data. Section 2 describes these methods as well as the data used in the study. Section 3 characterizes the patterns of first baroclinic mode ER waves and their relationship to the ISO, Section 4 investigates the processes modulating the upper OHC and zonal momentum of ER waves, and Section 5 provides a summary of the results.

2. Methodology

2.1. Data

ER wave composites of observed and reanalysis fields are shown throughout the investigation. The composite analysis is based on an index derived from satellite observations of sea surface height (SSH) anomalies from the Archiving, Validation, and Interpretation of Satellite Oceanographic (AVISO) level 4 reanalysis data set (Pascual et al., 2006). The SSH anomalies are available as daily averages on a 0.25° horizontal grid. Observations used in the composites include sea surface temperature (SST) from the National Oceanic and Atmospheric Administration (NOAA) daily optimum interpolation V2 (0.25°) (Reynolds et al., 2007), daily zonal pseudostress (0.25°) calculated as $u|\bar{u}|$ from the European Center for Medium Range Weather Forecasts Version 5 Reanalysis 10 m zonal winds (Hersbach et al., 2020), daily outgoing longwave radiation (OLR) (1°) from the NOAA Climate Data Record (Lee, 2011), and surface currents ($1/3^\circ$; interpolated to daily) from the Ocean Surface Current Analysis Real-time (Bonjean & Lagerloef, 2002; ESR, 2009) data sets.

A state-of-the-art HYCOM reanalysis (Metzger et al., 2017) is also used to examine subsurface characteristic of ER waves, including processes contributing to the tendencies of OHC and zonal momentum. The main utility of the reanalysis data set is the availability of subsurface variables, such as temperature and currents, at daily intervals and fine horizontal grid spacing. Without such reanalysis products, we are unable to *fully* resolve the coherent propagation of subsurface signals associated with planetary waves in the ocean. HYCOM reanalysis is composed of 41 vertical layers and a horizontal grid spacing of ~ 9 km near the equator. The reanalysis covers the years 1994–2015 and uses surface forcing fields from the National Centers for Environmental Prediction Climate Forecast System Reanalysis (Saha et al., 2010). The reanalysis also assimilates observed fields such as SSH, SST, sea ice concentration, salinity, and temperature from in situ observations such as ships, buoys, expendable bathythermographs, CTDs, and Argo floats among others, as well as satellite retrievals.

2.2. Methods

Previous studies have used an atmospheric index of the ISO to examine intraseasonal ocean dynamics in the region. For example, Webber et al. (2010) and Webber, Stevens, et al. (2012) used an ISO index based on OLR (Matthews, 2008), to investigate downwelling ER waves that force the initiation of primary ISO events in the western Indian Ocean. We investigate intraseasonal atmosphere-ocean interactions using an objective

index that identifies ocean ER waves using satellite observations of SSH, instead of an ISO index based on atmospheric variables (i.e., Kikuchi et al., 2012; Kiladis et al., 2014; Matthews, 2008; Wheeler & Hendon, 2004). Because of this, we more precisely identify processes determining intraseasonal OHC variability associated with ER waves, a limitation of Rydbeck, Jensen, Smith, et al. (2019) that used an OLR-based ISO index. In showing that systematic relationships between intraseasonal modes in the atmosphere and ocean hold regardless of the identifying index used, we increase confidence that these connections are not simply the result of selection criteria bias.

To isolate variability associated with intraseasonal ER waves, a newly developed ER wave index is employed using methods similar to those in a recent study of intraseasonal Kelvin waves in the equatorial Pacific Ocean (Rydbeck, Jensen, & Flatau, 2019) and also those routinely used in identification and classification of the ISO (e.g., Kiladis et al., 2014; Wheeler & Hendon, 2004). In short, this method filters SSH anomalies in wavenumber-frequency space to isolate the ER wave variability of interest. The leading pair of empirical orthogonal functions (EOFs) of the filtered SSH data describe the westward propagating first baroclinic mode ER wave, and the associated principal components (PCs) are used to characterize the wave's phase and amplitude. Composites are then generated for waves of sufficient amplitude and similar phasing in order to describe the wave's lifecycle. Details of the index are described below.

The ER wave index is based on AVISO SSH anomalies from 1993 to 2018. We remove the first three harmonics of the seasonal cycle, then filter to retain variability with 30–150-day periods and stationary/westward wavenumbers (i.e., those less than or equal to zero). The EOFs are calculated in the region of 6°S–6°N, 50°E–95°E in order to capture the salient characteristics and maximize the variance explained. While the variance explained decreases when the region is expanded, the leading features of the EOF analysis remain the same when latitude bounds are extended to 10°S/N and longitude bounds to 45°E and 105°E, respectively. The linear regression of AVISO SSH anomalies onto the first two PCs are shown in Figure 1 and represent the physical patterns of the leading EOFs with units of cm. The leading EOFs display SSH maxima/minima that are quasi-equatorially symmetric and located near the latitudes of +/- 4°. The first two EOFs are separable from lower modes according to the criterion of North et al. (1982) (Figure 2a) and when combined describe 41% of the westward propagating, intraseasonal variability in the equatorial Indian Ocean. The corresponding PCs have a correlation of 0.88 (–0.91) when PC2 leads (lags) PC1 by 21 days (Figure 2b), indicating that the modes describe the westward propagation of SSH anomalies. The PCs are also characterized by statistically significant spectral power at periods of 90 days (Figures 2c and 2d). The periodicity, phase direction, latitudes of propagation, and SSH signature correspond to first baroclinic mode ER waves.

A central utility of the EOF/PC pair is the generation of phase and amplitude descriptors of intraseasonal ER waves using the following formula:

$$\text{Amplitude}(t) = \sqrt{\text{PC1}(t)^2 + \text{PC2}(t)^2} \quad (1)$$

$$\text{Phase}(t) = \tan^{-1}\left(\frac{-\text{PC1}(t)}{-\text{PC2}(t)}\right) \quad (2)$$

The amplitude and phase information are used to generate composites of ER waves that represent the wave's entire lifecycle. Phases are discretized into eight bands of 45° phase widths such that each phase represents ~11 days of the wave's 90-day lifecycle. For each phase, ER waves that exceed 1.5 standard deviations are used for averaging in the composites. Intraseasonal anomalies shown in the composites are calculated by removing the first three harmonics of the seasonal cycle and applying a 30–150-day bandpass filter.

Statistical significance of the composite mean of intraseasonal anomalies for each phase is calculated using a two-tailed single sample *t*-test. A moving-blocks bootstrap with replacement is utilized to calculate the sample standard deviation used in the significance testing. A full description of this method is provided in Henderson et al. (2016) and is briefly described here. We first take the full record (1993–2018) of the variable and divide it into overlapping segments of block length *l*. The block length is calculated as the number of days in each phase, *N*, divided by the number of independent events in each phase. The number of independent events per phase is calculated by grouping consecutive days together such that they count as a single event. The block length is rounded to the nearest integer. For ER wave phases 1–8, the respective block

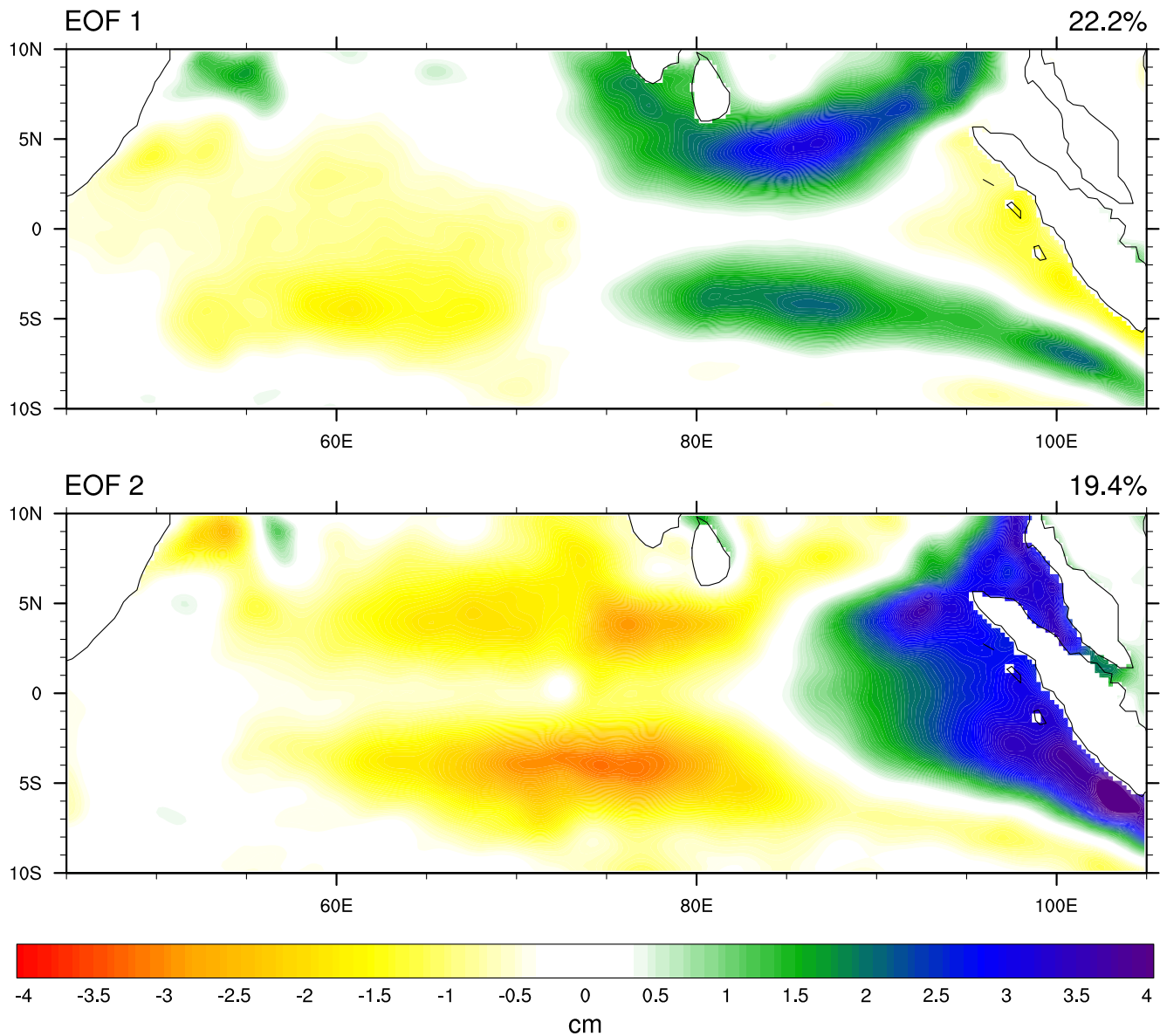


Figure 1. Linear regressions of unfiltered Archiving, Validation, and Interpretation of Satellite Oceanographic sea surface height (cm) anomalies onto the two leading principal components (multiplied by -1) are shown to represent the physical patterns of the leading empirical orthogonal functions (EOFs) with percent variance explained by each EOF in the upper right above each panel.

lengths are 7, 10, 11, 8, 7, 11, 12, and 7 days. To create a bootstrap sample of size N , we randomly sample and join N/l blocks of event data. This process is repeated 5,000 times to create bootstrap samples from which the sample standard deviation is calculated.

3. ER Waves

In this section, we examine the behavior of ER waves in the tropical Indian Ocean including their generation, maturation, and termination. Rossby waves are central to the evolution of the Indian Ocean Dipole through their modulation of the thermocline in the western Indian Ocean (Chowdary et al., 2009; Han et al., 1999; Murtugudde et al., 2000; Nagura & McPhaden, 2010; Vinayachandran et al., 1999, 2002, 2009) but are examined here in the context of the atmospheric ISO. Of particular interest is the relationship of ER waves to deep atmospheric convection and associated wind stress. We investigate the timing of these

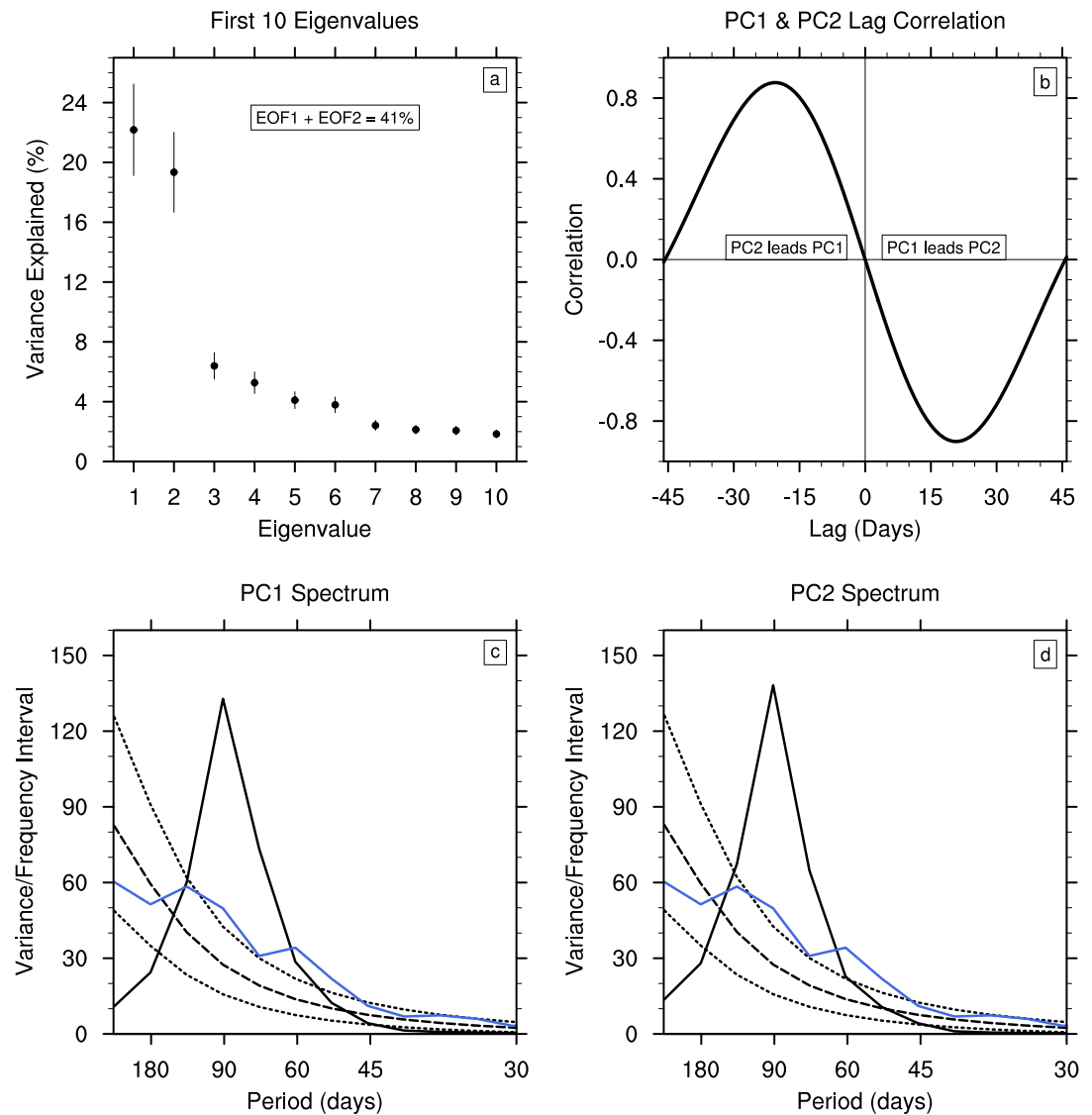


Figure 2. The (a) variance explained by the first 10 empirical orthogonal functions (EOFs) (dots) with standard errors (lines), (b) lag correlation of the leading principal components (PCs), (c) power spectrum of the first PC (black), and (d) power spectrum of the second PC (black) are shown. The power spectra (c and d) are shown with the 99% and 1% upper and lower significance levels (dotted lines) and the red noise spectrum (dashed lines). The blue line in panels (c and d) represents the background subseasonal sea surface height (SSH) spectrum taken from SSH anomalies filtered to retain periods less than 400 days.

features in relation to one another, and attempt to diagnose feedbacks between them. These relationships are shown as a function of the ER wave index described in Section 2.2.

3.1. General Characteristics

Following the work of Rydbeck, Jensen, Smith, et al. (2019), we investigate ER waves hypothesized to regulate OHC in the tropical Indian Ocean during the ISO. The evolution of the first baroclinic mode ER wave is shown using intraseasonal anomalies of SSH and surface currents (Figure 3). Increases in SSH are associated with ocean downwelling which depresses the thermocline and, in turn, increases the upper OHC which raises the height of the sea surface. Downwelling (upwelling) waves are indicated by positive (negative) SSH anomalies. Phases 1 and 2 show the waning of upwelling waves in the central Indian Ocean and concomitant weakening of eastward currents along the equator. At the same time, downwelling waves

ER Wave SSH (shading) and Currents (vectors)

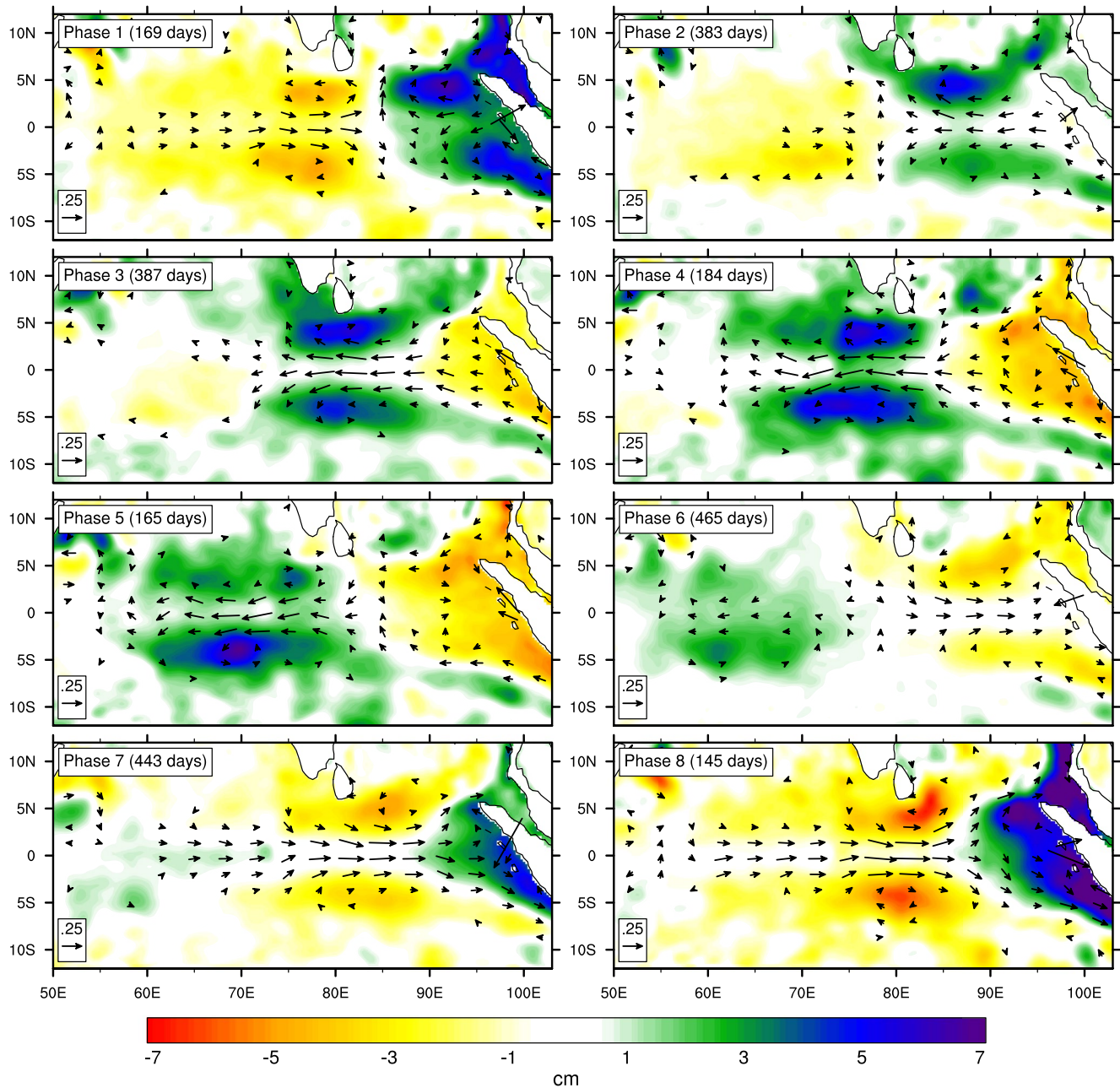


Figure 3. Composite maps of the 30–150-day band-pass-filtered Archiving, Validation, and Interpretation of Satellite Oceanographic sea surface height (SSH) (shading, cm) and Ocean Surface Current Analysis Real-time surface currents (vector, m/s) anomalies based on the equatorial Rossby (ER) wave index are shown for phases 1–8. The number of days in each phase composite is shown in the upper left, and the reference current vector is shown in the bottom left of each panel.

near the Sumatra coast and westward currents along the equator are developing and propagating westward. Anomalous SSHs increase in magnitude to 6 cm and westward currents accelerate to 50 cm s^{-1} , while continuing their propagation westward into the central Indian Ocean during phases 3 and 4. The downwelling wave in the northern hemisphere weakens in phase 5, likely owing to interactions with Sri Lanka and the Maldives. Upwelling waves that flank an anomalous eastward current along the equator begin to propagate away from the Sumatra coast in phase 6, and intensify in phases 7 and 8.

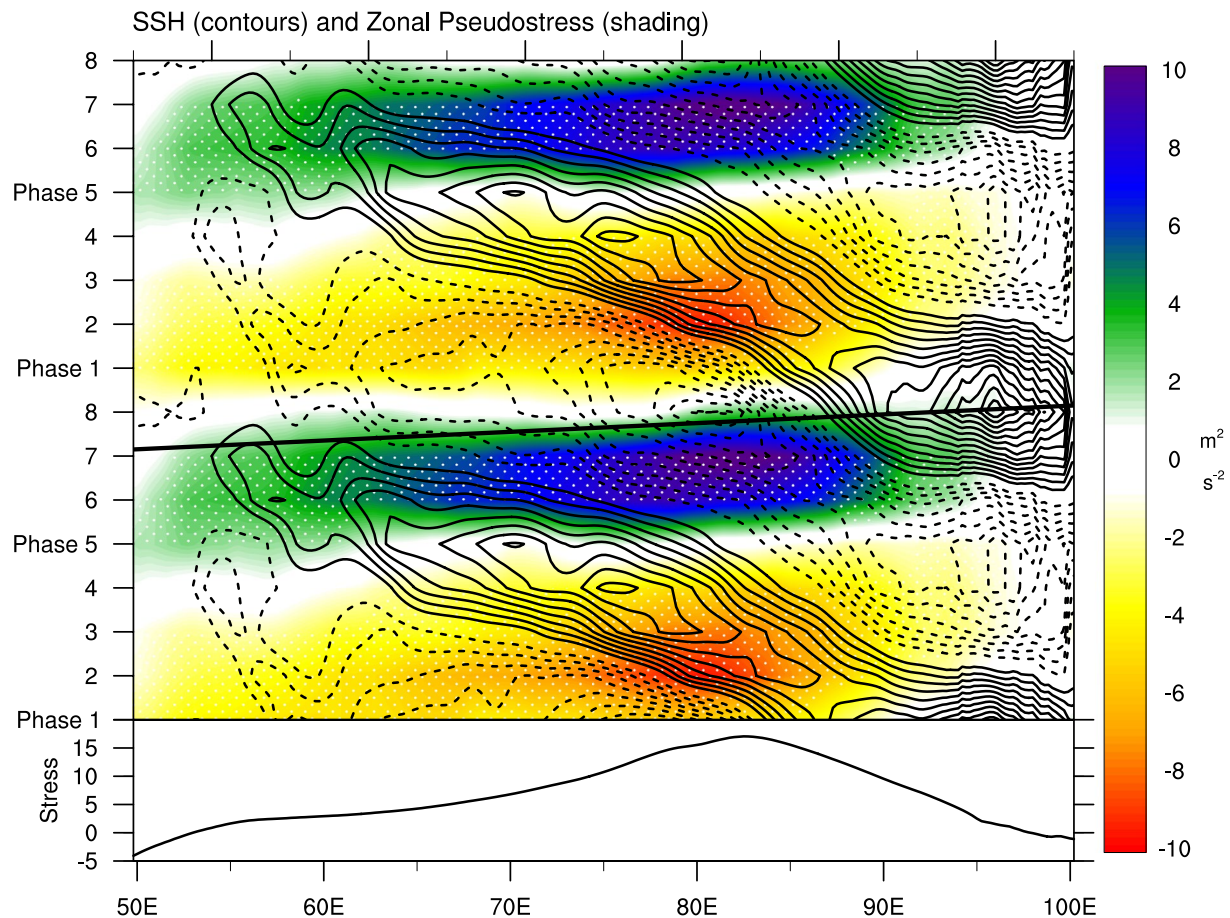


Figure 4. Composite of 30–150-day band-pass-filtered Archiving, Validation, and Interpretation of Satellite Oceanographic sea surface height (SSH) (contours, cm) and ERA5 zonal pseudostress (shading, $\text{m}^2 \text{s}^{-2}$) anomalies based on the equatorial Rossby wave index are shown for phases 1–8. SSH anomalies are averaged from 2° to 6°S and 2° to 6°N . Solid (negative) contours are positive (dashed). The contour interval is 0.5 cm and omits the zero-contour line. Zonal pseudostress anomalies are averaged from 5°S to 5°N . Climatological zonal pseudostress averaged from 5°S to 5°N is shown in the bottom panel. White stippling indicates zonal pseudostress values significantly different from zero at the 99% confidence threshold. The black line indicates a phase speed of 6.9 m s^{-1} .

Downwelling waves propagate farther to the west with greater intensity than their upwelling counterparts. This behavior also extends to the equatorial zonal currents, suggesting a preferred maintenance mechanism for downwelling versus upwelling waves. We investigate this in Section 4.2 where the terms contributing to the momentum tendency of the equatorial zonal currents are quantified and examined. We briefly examine one possible mechanism here. Figure 4 shows the intraseasonal zonal wind stress and SSH anomalies as a function of phase and longitude. Wind stress anomalies are averaged from 5°S to 5°N while SSH anomalies are averaged for the latitude bands 2° – 6°N and 2° – 6°S in order to isolate the SSH maxima and minima shown in Figure 3. Westerly (easterly) wind stress anomalies of $10 \text{ m}^2 \text{ s}^{-2}$ ($-9 \text{ m}^2 \text{ s}^{-2}$) immediately precede the generation of downwelling (upwelling) ER waves along the eastern boundary during phases 6 and 7 (2 and 3). These ER waves are likely generated by the reflection of downwelling Kelvin waves that are forced by the eastward propagating wind stress anomalies. In this study, the procedure of compositing for westward propagating ER waves excludes eastward propagating Kelvin wave variability.

However, the generation of Kelvin waves by eastward propagating intraseasonal wind stress, like that shown in Figure 4, is well documented (Fu, 2007; Han, 2005; Iskandar & McPhaden, 2011; Iskandar et al., 2005; Jensen et al., 2015; Pujiana & McPhaden, 2020; Sengupta et al., 2007; Shinoda et al., 2013; Vialard et al., 2009). Downwelling ER waves then propagate westward, encountering a region of strong anomalous easterly wind stress between 80° and 85°E and phases 1–3 which accelerates the westward zonal current. A similar process occurs for upwelling waves and the respective eastward zonal currents. A primary difference between the easterly and westerly zonal wind stress anomalies is their duration. Easterly wind

stress anomalies persist for approximately 4.5 phases while westerly wind stress anomalies persist for 3.5 phases, indicating that westward currents and downwelling ER waves are supported by more enduring local wind forcing (~ 50 vs. ~ 39 days).

3.2. Synchronization With the ISO

A remarkable feature of Figure 4 is the synchronization of intraseasonal zonal pseudostress and SSH anomalies in the equatorial Indian Ocean indicative of a systematic relationship between ISO amplification and ER wave generation and maintenance. Near 100°E , the generation of upwelling and downwelling ER waves is coincident with negative and positive pseudostress anomalies, respectively. The upwelling and downwelling waves also reach peak amplitude shortly after the pseudostress maximum and minimum cross the ER wave path near 80°E . Pseudostress anomalies in Figure 4 propagate eastward with a phase speed of 6.9 m s^{-1} indicated by the black line. This is slightly faster than the ISO (5.0 m s^{-1}) (Knutson & Weickmann, 1987; Weickmann et al., 1985) but slower than that of a convectively coupled Kelvin wave ($15\text{--}20\text{ m s}^{-1}$) (Straub & Kiladis, 2002; Wheeler & Kiladis, 1999). This is also faster than the “fast” modes of the ISO (5.5 m s^{-1}) (Wang et al., 2019), perhaps suggesting an amalgam of ISO and convectively coupled Kelvin wave modes in the composite stress (Roundy, 2020).

Intraseasonal OLR anomalies are likewise synchronized with ER waves (Figure 5). While statistically significant OLR anomalies are present across the entire equatorial Indian Ocean, the OLR minimum representative of enhanced convection occurs immediately after passing over the anomalous SSH maximum near phase 4 at 76°E . In other words, enhanced atmospheric convection intensifies after propagating over the maximum amplitude of the downwelling ER wave, perhaps indicating a positive ocean-atmosphere feedback. This relationship holds even when composites are partitioned by season (figure not shown). This proposed feedback is systematically investigated using budgets of the OHC tendency in Section 4.1. The composite of intraseasonal OLR anomalies indicates a phase speed of 4.7 m s^{-1} , broadly consistent with the eastward propagation speed of the ISO. Composites of intraseasonal OLR and pseudostress anomalies weaken as they approach the Maritime Continent, and only the stress anomalies appreciably re-strengthen in the west Pacific Ocean (not shown).

To note, statistically significant OLR anomalies are present in the western equatorial Indian Ocean, prior to the arrival of downwelling ER waves there. This indicates that while the downwelling ER waves identified in this analysis might assist the rapid strengthening of the ISO, they are not typically responsible for its initiation. This does not rule out the possibility of ISO convective initiation by downwelling ER waves as shown in previous work (Rydbeck & Jensen, 2017; Rydbeck, Jensen, & Flatau, 2019; Rydbeck, Jensen, & Igel, 2019; Webber et al., 2010; Webber, Matthews, et al., 2012; Webber, Stevens, et al., 2012; West et al., 2018, 2020), but suggests that this behavior is atypical as indicated by compositing over many ER wave events. It should be noted that ER waves discussed here are just one factor amongst many that have shown to vary the intensity of the ISO. Others include, but are not limited to, the horizontal distribution of atmospheric moisture (e.g., Adames & Wallace, 2015; Hsu & Li, 2012), wind-induced surface heat exchanges (e.g., Emanuel, 1987; Neelin et al., 1987), atmospheric frictional convergence (e.g., Lau & Peng, 1987), atmospheric radiative heating (e.g., Del Genio & Chen, 2015; Raymond, 2001), and diurnal variability (e.g., Ruppert & Johnson, 2015).

Rydbeck, Jensen, Smith, et al. (2019) hypothesized that OHC anomalies favorably align with intraseasonal convection due to the serendipitous phasing of ER waves forced by successive ISO events. Positive intraseasonal OHC anomalies are hypothesized to mitigate the SST cooling that routinely occurs during convectively active ISO periods. Without the enhanced OHC, SST cooling would be stronger, reducing surface latent and sensible heat fluxes and, as a result, the intensity of ISO convection. We provide support in subsequent sections that the systematic phase alignment of the ISO and OHC is, in fact, due to the generation of and maintenance of first baroclinic mode ER waves forced by ISO events. For our purposes, OHC is defined as the integrated temperature excess above 26°C (299.15 K), commonly referred to as tropical cyclone heat potential, and is computed from HYCOM reanalysis data using the following formula,

$$\text{OHC} = \rho c_p \int_{Z_{26^\circ\text{C}}}^{\text{Surface}} (T(z) - 299.15\text{ K}) dz \quad (3)$$

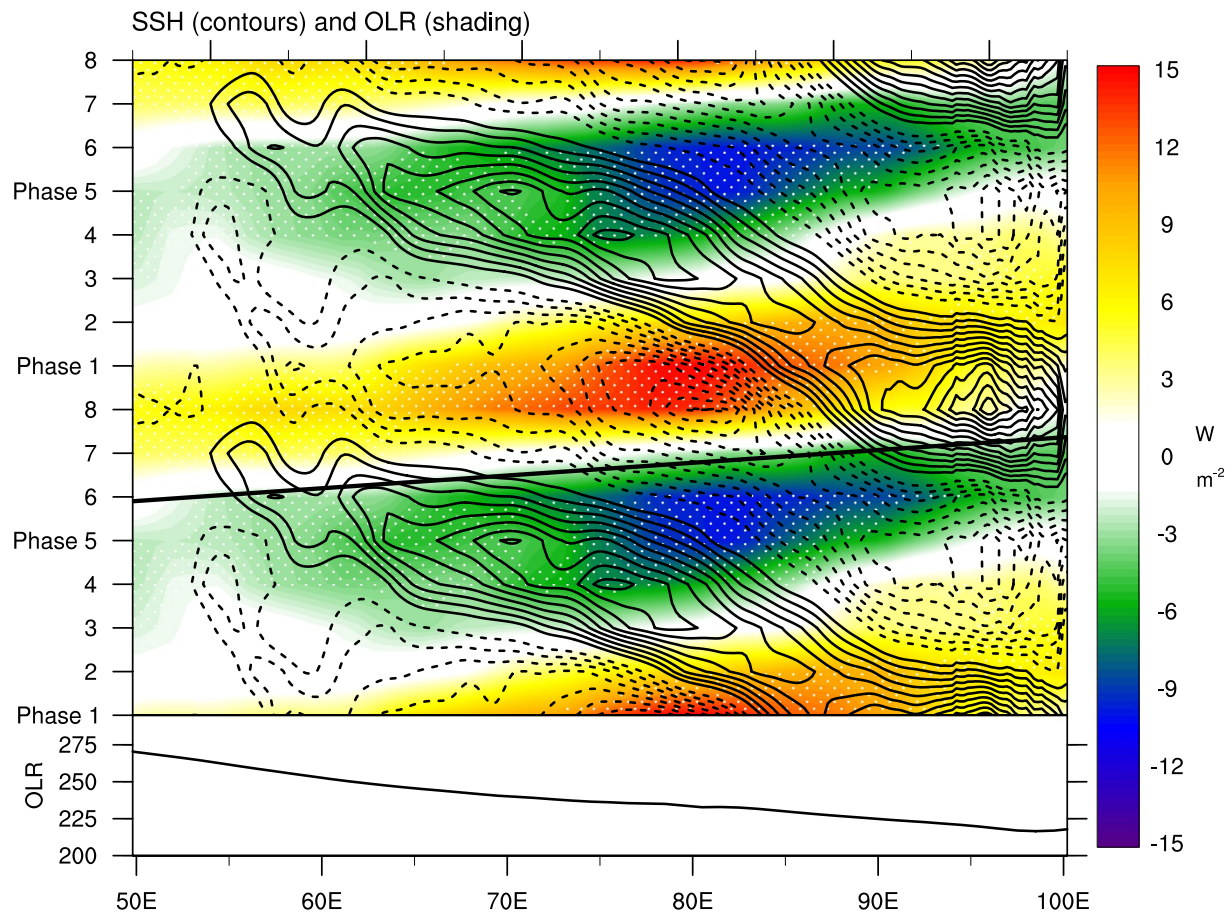


Figure 5. Composite of 30–150-day band-pass-filtered Archiving, Validation, and Interpretation of Satellite Oceanographic sea surface height (SSH) (contours, cm) and National Oceanic and Atmospheric Administration Climate Data Record outgoing longwave radiation (OLR) (shading, W m^{-2}) anomalies based on the equatorial Rossby wave index are shown for phases 1–8. SSH anomalies are averaged from 2° to 6°S and 2° to 6°N . Solid (negative) contours are positive (dashed). The contour interval is 0.5 cm and omits the zero contour line. OLR anomalies are averaged from 10°S to 10°N . Climatological OLR averaged from 10°S to 10°N is shown in the bottom panel. White stippling indicates OLR values significantly different from zero at the 99% confidence threshold. The black line indicates a phase speed of 4.7 m s^{-1} .

where ρ is the density of seawater ($1,027 \text{ kg m}^{-3}$), c_p is the specific heat of seawater at constant pressure ($3,986 \text{ J kg}^{-1} \text{ K}^{-1}$), $T(z)$ is the temperature in Kelvin as a function of depth, and $Z_{26^{\circ}\text{C}}$ is the depth of the 26°C isotherm. OHC units are shown in kJ cm^{-2} .

Intraseasonal OHC anomalies coherently propagate westward and are phase aligned with SSH anomalies that define the ER wave, indicating that SSH anomalies are a good proxy for intraseasonal ER OHC variability (Figure 6). Maxima and minima of OHC anomalies are $\pm 15\%$ of the mean OHC magnitude, with statistically significant anomalies present across most of the basin along the ER wave path. The anomalous OHC maximum occurs near 76°E during phase 4 while the minimum is located at 82°E during phase 8. The maximum of OHC occurs in a similar region and 1 phase earlier than the rapid decrease of OLR (increase of convection) shown in Figure 5. The anomalous increase of OHC prior to the enhancement of intraseasonal convection agrees with the study of Rydbeck, Jensen, Smith, et al. (2019). In that study, they discovered an increase of OHC along the equator prior to and during the intensification of ISO convection in the central Indian Ocean using an ISO index based on OLR anomalies (Kiladis et al., 2014). Regardless of whether the intraseasonal index used for compositing is based on leading modes of atmospheric convection as in Rydbeck, Jensen, Smith, et al. (2019) or SSH as in the present study, similar phase alignments between OLR and OHC anomalies are observed and suggestive of large scale, intraseasonal atmosphere-ocean reciprocation.

The evolution of SST anomalies (Figure 7) exhibits important differences from the OHC anomalies. Significant anomalies do not extend west of 75°E and do not coherently propagate with SSH anomalies across

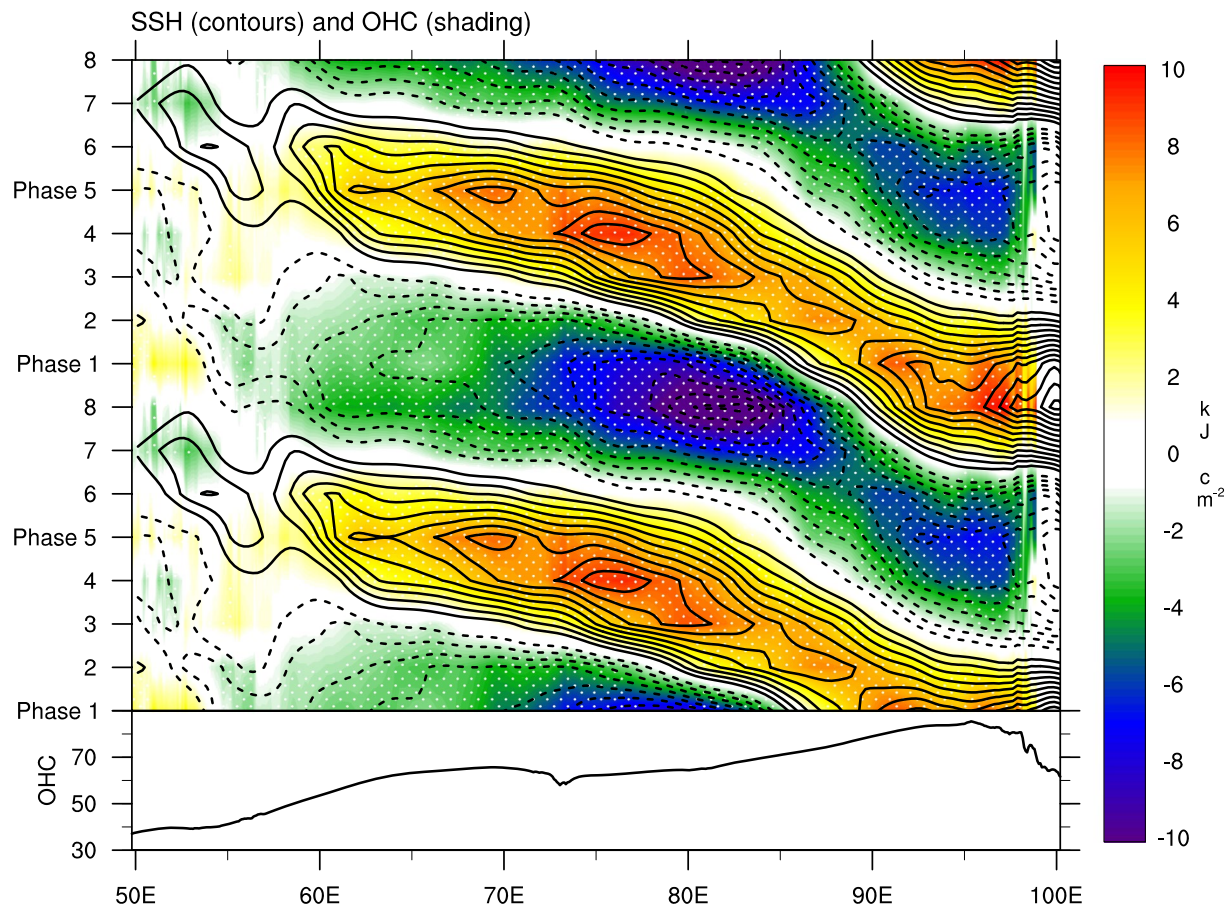


Figure 6. Composite of 30–150-day band-pass-filtered Archiving, Validation, and Interpretation of Satellite Oceanographic sea surface height (SSH) (contours, cm) and HYCOM ocean heat content (shading, kJ cm^{-2}) anomalies based on the equatorial Rossby wave index are shown for phases 1–8. Data from 1994 to 2015 are shown. SSH and ocean heat content anomalies are averaged from 2° to 6°S and 2° to 6°N . Solid (negative) contours are positive (dashed). The contour interval is 0.5 cm and omits the zero contour line. Climatological ocean heat content averaged from 2° to 6°S and 2° to 6°N is shown in the bottom panel. White stippling indicates ocean heat content values significantly different from zero at the 99% confidence threshold.

the entire basin like OHC anomalies. The anomalous SST maximum and minimum of $\pm 0.15^\circ\text{C}$ occur near 81°E . Positive SST anomalies occur during periods of downwelling waves while negative SST anomalies generally occur during upwelling waves. The maxima and minima of SST anomalies occur in advance of atmospheric OLR anomalies (see Figure 5), and previous studies have shown that atmospheric heat flux forcing associated with anomalous convection strongly modulates SST (DeMott et al., 2015 and references therein). The locations of the SST maxima/minima are broadly consistent with those of OHC anomalies. The quasi-stationary character of the SST anomalies perhaps results from competing eastward and westward propagation mechanisms, like horizontal advection (i.e., westward) and surface flux forcing (i.e., eastward). Future work will focus on the dependencies of SST anomalies on intraseasonal variations of OHC and the degree to which OHC retards the rate of cooling during convectively enhanced phases of the ISO.

Composite maps also show important latitudinal variations of intraseasonal SST anomalies (Figure 8). Maxima and minima tend to occur at similar latitudes as the ER waves and are somewhat phase aligned with the SSH anomalies. During phases 3 and 7, broad warming and cooling is present across the equatorial Indian Ocean in association with the respective downwelling and upwelling ER wave phases. While much of this behavior might be associated with the alternating convective phases of the ISO that are synchronous with the ER waves, it is notable that the maxima and minima are generally located within the SSH envelope of the ER waves. When the downwelling wave is weakened in the northern hemisphere during phase 5, the magnitude of warming there also weakens. This behavior might be expected if the magnitude of downwelling is proportional to the degree of surface warming, for example, by the suppression of vertical mixing.

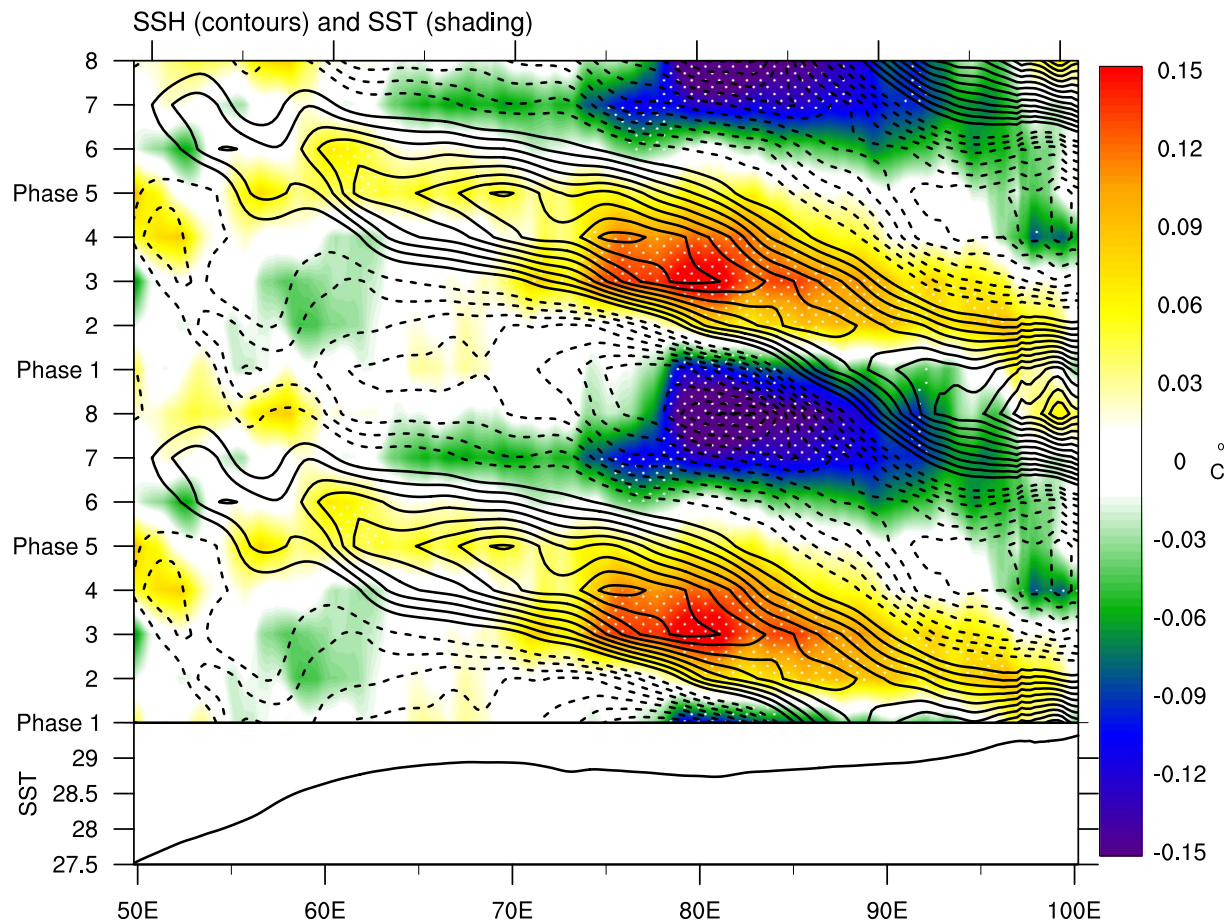


Figure 7. Composite of 30–150-day band-pass-filtered Archiving, Validation, and Interpretation of Satellite Oceanographic sea surface height (SSH) (contours, cm) and National Oceanic and Atmospheric Administration sea surface temperature (SST) (shading, °C) anomalies based on the equatorial Rossby wave index are shown for phases 1–8. SSH and SST anomalies are averaged from 2° to 6°S and 2° to 6°N. Solid (negative) contours are positive (dashed). The contour interval is 0.5 cm and omits the zero contour line. Climatological SST averaged from 2° to 6°S and 2° to 6°N is shown in the bottom panel. White stippling indicates SST values significantly different from zero at the 99% confidence threshold.

More work is required to understand the modulating effect of ER waves on SST in the presence of strong atmospheric forcing. We reserve in-depth investigations of SST variability for future work and instead focus on intraseasonal OHC anomalies.

4. ER Wave Tendencies

Specific mechanisms responsible for the harmonization of ER waves and the ISO are not fully known. In an attempt to disentangle the interplay between intraseasonal modes in the atmosphere and ocean, terms of the OHC and zonal momentum budgets are composited as a function of ER wave phase. The respective budgets are presented in this section.

4.1. OHC Tendency

The evolution of temperature as a function of depth, longitude, and ER wave phase is shown in Figure 9. In the eastern equatorial Indian Ocean, warm anomalies rapidly develop along the thermocline in phase 7 with a maximum of 0.75°C. These anomalies extend westward and intensify with the maximum exceeding 1.2°C during phase 8. The anomalies propagate westward and gradually weaken from 0.9°C to 0.45°C from phase 1 to 3. The anomalies re-intensify to 0.75°C in the central Indian Ocean near 74°E during phases 4 and 5, and then weaken again as they continue propagating westward. By phase 7, the warm anomalies

ER Wave SSH (contours) and SST (shading)

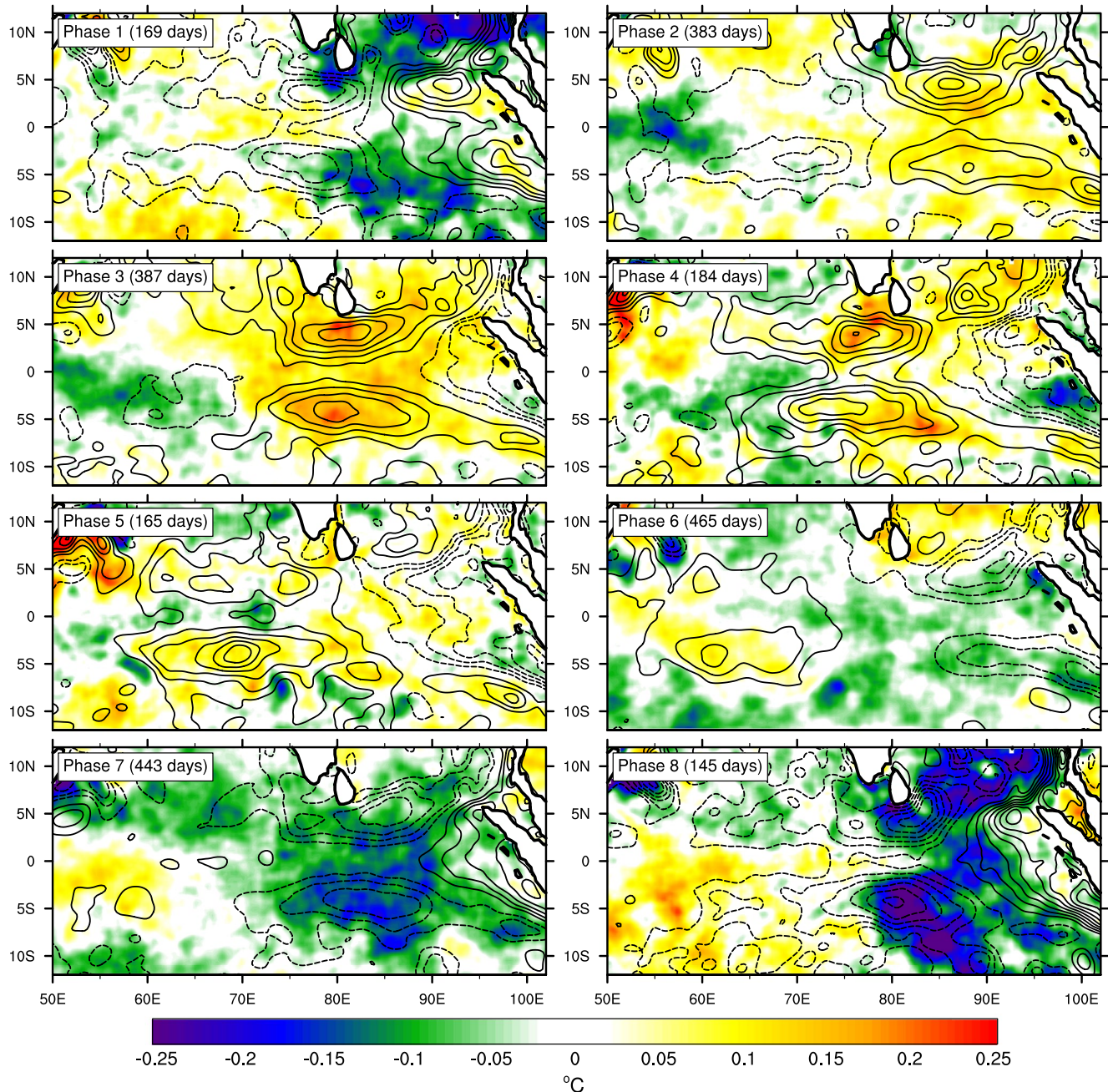


Figure 8. Composite maps of the 30–150-day band-pass-filtered Archiving, Validation, and Interpretation of Satellite Oceanographic sea surface height (SSH) (contours, cm) and National Oceanic and Atmospheric Administration sea surface temperature (SST) (shading, °C) anomalies based on the equatorial Rossby (ER) wave index are shown for phases 1–8. Solid (negative) contours are positive (dashed). The contour interval is 1 cm and omits the zero contour line. The number of days in each phase composite is shown in the upper left.

become less coherent in the western Indian Ocean and are absent by phase 8. The intensification in the eastern Indian Ocean at phase 7 and the reamplification of anomalies in the central Indian Ocean are the focus of the OHC budget analyses shown next. In particular, we are interested in determining the quantitative contribution of atmospheric processes versus ocean dynamics to the intraseasonal variations of OHC.

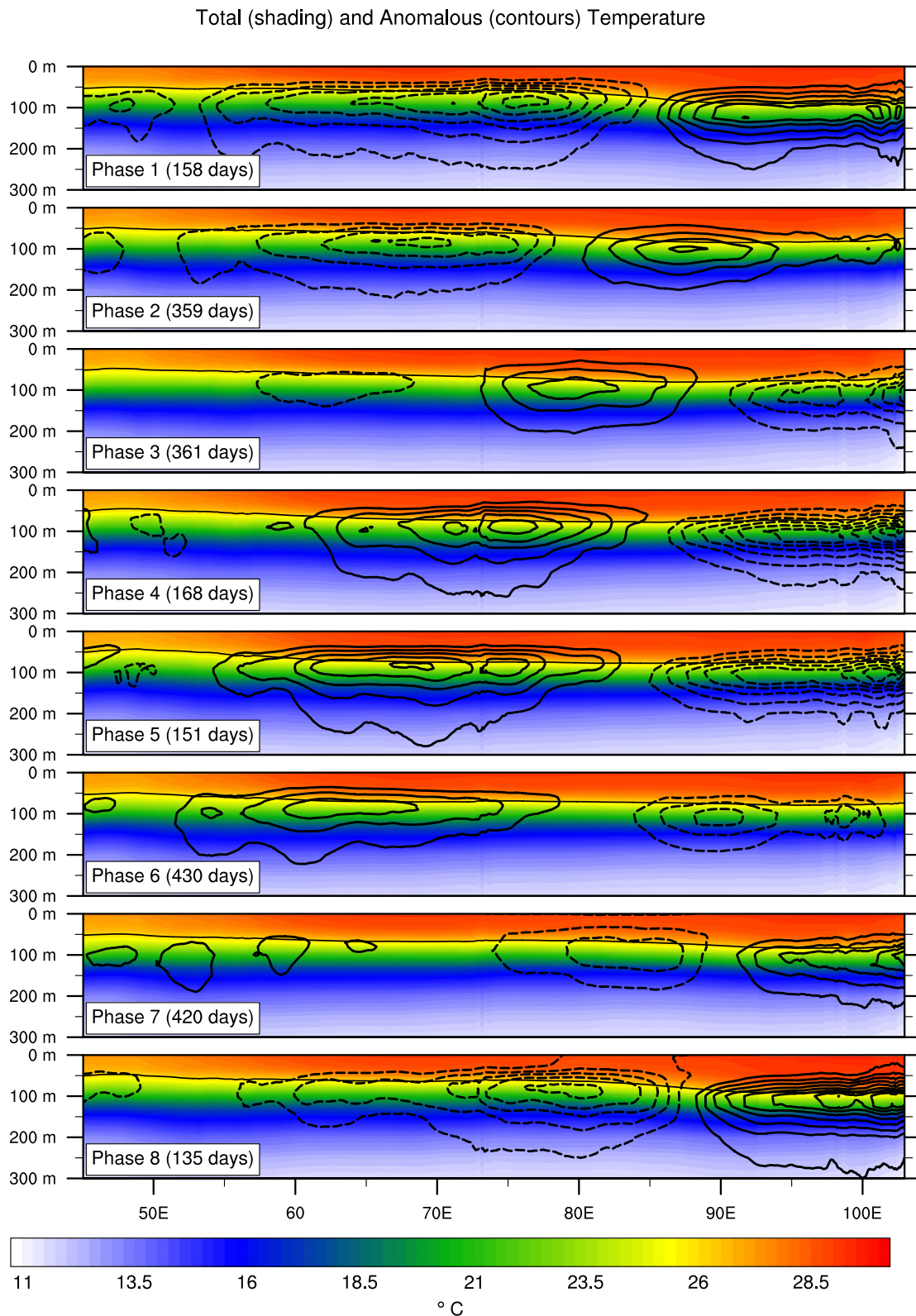


Figure 9. Composite of unfiltered HYCOM temperature (shading, °C) and 30–150-day band-pass-filtered temperature anomalies (contours, °C) based on the equatorial Rossby wave index are shown for phases 1–8. Data from 1994 to 2015 are shown. Temperatures are averaged from 6°S to 6°N. Solid (negative) contours are positive (dashed). The contour interval is 0.15°C and omits the zero contour line. The number of days in each phase composite is shown in the bottom left. The thin black line indicates the 26°C isotherm.

OHC is a measure of the ocean's internal energy. Under conditions of strong air-sea interactions, OHC quantifies the ocean's thermodynamic resistance to temperature changes resulting from fluxes across the upper and lower boundaries of the integrating layer. The OHC tendency and forcing terms are calculated using the following formula,

$$\begin{aligned}
 \underbrace{(\partial\text{OHC}/\partial t)'}_1 &= \left(\rho C_p \partial \left(\int_{Z_{26^\circ\text{C}}}^0 T \partial z \right) / \partial t \right)' \\
 &= - \underbrace{\left(\rho C_p \int_{Z_{26^\circ\text{C}}}^0 U_H \cdot \nabla T \partial z \right)'}_2 - \underbrace{\left(\rho C_p \int_{Z_{26^\circ\text{C}}}^0 A_H \nabla^2 T \right)'}_3 - \underbrace{\left(\rho C_p \int_{Z_{26^\circ\text{C}}}^0 w \frac{\partial T}{\partial z} \partial z \right)'}_4 \\
 &\quad - \underbrace{\left(\rho C_p Z_{26^\circ\text{C}} \frac{\partial Z_{26^\circ\text{C}}}{\partial t} \frac{\partial T}{\partial z} \Big|_{Z_{26^\circ\text{C}}} \right)'}_5 - \underbrace{\left(\rho C_p A_z \frac{\partial T}{\partial z} \Big|_{Z_{26^\circ\text{C}}} \right)'}_6 + \underbrace{(\text{LH})_0'}_7 + \underbrace{(\text{SH})_0'}_8 \\
 &\quad + \underbrace{(\text{LW})_0'}_9 + \underbrace{(\text{SW})_0 - \text{SW}|_{Z_{26^\circ\text{C}}}}_{10}
 \end{aligned} \tag{4}$$

In this formula, T is the ocean temperature, $Z_{26^\circ\text{C}}$ is the depth of the 26°C isotherm, U_H is the horizontal ocean velocity, A_H is the horizontal eddy diffusivity ($1.5 \times 10^{-3} \text{ m}^2 \text{ s}^{-1}$), A_V is the vertical eddy diffusivity ($1.0 \times 10^{-5} \text{ m}^2 \text{ s}^{-1}$), LH is the latent heat flux, SH is the sensible heat flux, LW is the longwave radiative flux, and SW is the shortwave radiative flux. The shortwave radiative flux evaluated at the 26°C isotherm depth is the flux that penetrates the base of OHC integrating layer and is calculated using the method of (Pacanowski & Griffies, 2000). Primed terms indicate intraseasonal anomalies. Term 1 is the temporal tendency of intraseasonal OHC anomalies, term 2 is the horizontal advection of OHC anomalies, term 3 is the horizontal eddy diffusion of OHC anomalies, term 4 is the vertical advection of OHC anomalies, term 5 is the vertical entrainment of OHC anomalies due to changes in the depth of the 26°C isotherm, and term 6 is the vertical eddy diffusion of OHC anomalies across the base of the integrating layer. Terms 7, 8, 9, and 10 are the tendencies resulting from surface latent heating, surface sensible heating, surface longwave radiative flux, and the net shortwave radiative flux, respectively. Because the calculation of vertical velocities by use of the continuity equation, and by extension the vertical advection, is intractable using HYCOM reanalysis data that has been interpolated from the native model vertical grids to z -levels, the vertical advection is calculated as the budget residual.

Terms of the OHC tendency equation are shown in Figure 10. The phase of each tendency term in relation to the anomalous OHC shown in the black contours is of great importance. If the tendency term and OHC are in phase, it indicates that the term is increasing the magnitude of the OHC anomalies. If they are out of phase, the term is decreasing the OHC. If the terms lead the OHC anomalies by 2 phases ($1/4$ of the ER wave lifecycle), it results in a propagation of the anomalies toward the location of the tendency term. The tendency term can also be a combination of these effects such that it modulates the amplitude while also propagating the anomalies. This framework for viewing the budget terms in which they are referenced as in/out of phase or leading/lagging the anomalies is also used when investigating the zonal momentum tendency (Section 4b). Horizontal and vertical diffusion are minor contributors to the budget and included in the horizontal and vertical advection terms, respectively. Terms are averaged from 2° to 6°S and 2° to 6°N and shown as a function of the ER wave phase with black dots indicating the approximate longitude of the downwelling ER wave center.

The intraseasonal OHC tendency in the equatorial Indian Ocean during ER waves is a coordinated arrangement of atmospheric forcing propagating eastward and ocean forcing propagating westward. As the wave propagates from the eastern to western Indian Ocean, a positive OHC tendency coherently propagates in advance of the downwelling wave (Figure 10a). The wave is immediately followed by local maxima of OHC (solid line contours). The anomalous OHC maximum of 9 kJ cm^{-2} is located in the central Indian Ocean at 77°E , while the maximum OHC tendency of 45 W m^{-2} is located near 87°E . While this might seem perplexing at first, the maximum OHC is an integration of the anomalous OHC tendency, depending on both the amplitude and duration of the positive OHC tendency. The latter is important in determining the maximum

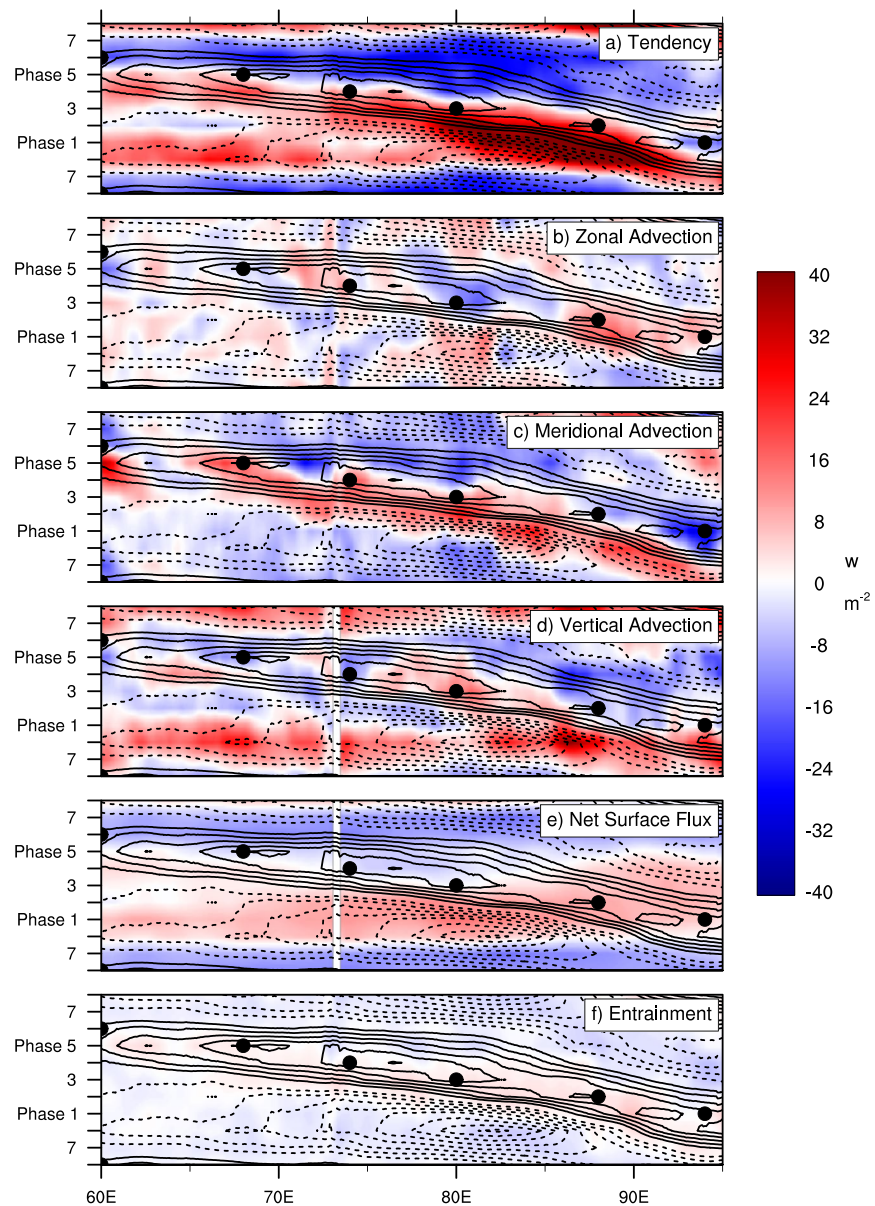


Figure 10. Composite of 30–150-day bandpass-filtered HYCOM ocean heat content anomaly tendency terms (shading, W m^{-2}) and 30–150-day band-pass-filtered ocean heat content anomalies (contours, kJ cm^{-2}) based on the equatorial Rossby wave index are shown for phases 1–8. Data from 1994 to 2015 are shown. The anomalous ocean heat content (a) tendency, (b) zonal advection, (c) meridional advection, (d) vertical advection, (e) net surface flux, and (f) entrainment are included. Values are averaged from 2° to 6°S and 2°S to 6°N . Positive (negative) contours are solid (negative) with an interval 1.5 kJ cm^{-2} , omitting the zero contour. Black dots indicate approximate location of downwelling equatorial Rossby wave center.

at 77°E . The OHC tendency generally weakens in the western Indian Ocean and becomes quasi-stationary. As we will show, the varying behavior of the OHC tendency between the eastern and western Indian Ocean is a result of counter propagating forcings in the atmosphere and ocean.

The westward propagation of ER waves is accompanied by anomalous meridional advection of OHC (Figure 10c) that is stronger and more coherent than zonal advection (Figure 10b). Positive meridional advection of OHC leads OHC anomalies by ~ 2 phases (22 days) in most of the Indian Ocean, indicating its primary role in propagating OHC anomalies westward. In certain regions, meridional advection is responsible for up to half (20 W m^{-2}) of the OHC tendency. While zonal currents have a strong signal along the equator

for ER waves, OHC anomalies are generally located off the equator such that the role of zonal advection is muted. The coherent westward propagation of meridional advection with the OHC anomalies highlights the important roles of ocean dynamics associated with ER waves in controlling their propagation.

Vertical advection generally increases anomalous positive OHC in the central Indian Ocean. In the central Indian Ocean, vertical advection is positive and in phase with positive OHC anomalies during phases 2–6 and 75°E–85°E, indicating its role in amplifying OHC there. The propagation of positive vertical advection tendencies with the downwelling ER wave in much of the eastern and central Indian Ocean suggest that it is intrinsic to the wave, in agreement with the findings of Effy et al. (2020). Vertical advection is also positive and collocated with negative OHC anomalies in the central and western Indian Ocean during phases 6–8 and phase 1 (Figure 10d), such that it reduces the magnitude of negative OHC anomalies. The local maxima of vertical advection that is coincident with the maximum of OHC in the central Indian Ocean near 77°E is the leading positive “in phase” tendency term for this location, indicating that vertical advection is the primary contributor to the increase of positive OHC anomalies there. This is important because of the relationship between OHC and atmospheric convection there shown in Figure 5. Atmospheric deep convection is enhanced 1 phase (~11 days) after the OHC maximum at the same longitude. From the analysis of vertical and meridional advection, we hypothesize that ocean dynamics associated with downwelling ER waves, which are shown to increase OHC, contributes to the maintenance and intensification of ISO convection in the central Indian Ocean.

Surface flux forcing displays prominent eastward propagation (Figure 10e), in contrast to the westward propagation of meridional and vertical advection (Figures 10c and 10d). Because the OHC anomalies are westward propagating and the surface flux anomalies are eastward propagating, the phase relationship between the two varies across the equatorial Indian Ocean. In the eastern Indian Ocean, OHC and surface flux anomalies are largely in phase, indicating that surface flux forcing increases the amplitude of OHC anomalies in this region. In the central Indian Ocean near 80°E, surface flux forcing is a maximum (15 W m^{-2}) and leads OHC anomalies by 1/4 cycle, indicating that they propagate the OHC anomalies. While weaker in the western Indian Ocean, the surface flux anomalies are largely out of phase with the OHC anomalies, such that they contribute to the overall decrease of OHC amplitude there. In summary, surface fluxes intensify OHC anomalies in the eastern Indian Ocean, propagate the anomalies in the central Indian Ocean, and decrease the magnitude of OHC anomalies in the western Indian Ocean.

The tendency due to vertical entrainment is modest ($\pm 0\text{--}5 \text{ W m}^{-2}$) and quasi-stationary in the central and western Indian Ocean where the term is most coherent. Entrainment is predominantly out of phase with the net surface heat flux, suggesting that atmospheric forcing is the leading contributor to variations of the 26°C isotherm depth that force entrainment/detrainment across the OHC integration layer. In general, entrainment strengthens the magnitude of negative OHC anomalies in the central and western Indian Ocean, acting in opposition to vertical advection.

To quantify the importance of net surface fluxes versus ocean dynamics (sum of horizontal advection, vertical advection, and entrainment) terms in the OHC tendency, the tracer balance metric of Halkides et al. (2015) is applied. This metric quantifies the dominant OHC forcing mechanism. This balance metric reveals that ocean dynamics are most important for the westward propagating positive OHC tendency that accompanies the downwelling ER wave and for the quasi-stationary positive OHC tendency in the central and western Indian Ocean (figure not shown). This metric further indicates the predominant role for ocean dynamics in determining intraseasonal OHC variations in the equatorial Indian Ocean during ER wave events.

4.2. Zonal Momentum Tendency

The OHC budget described in the previous section demonstrates the role of ocean dynamics associated with downwelling ER waves for increasing the OHC such that it assists the maintenance and intensification of ISO deep convection. The ocean zonal momentum budget shows the forcing of ER waves by ISO winds, completing the intraseasonal atmosphere-ocean feedback loop. The processes modulating the kinetic energy of ER waves in the equatorial Indian Ocean fall into two broad categories: (a) direct wind forcing and (b) preexisting energy reflecting at basin boundaries. Previous linear modeling and observational studies have

Total (shading) and Anomalous (contours) Zonal Currents

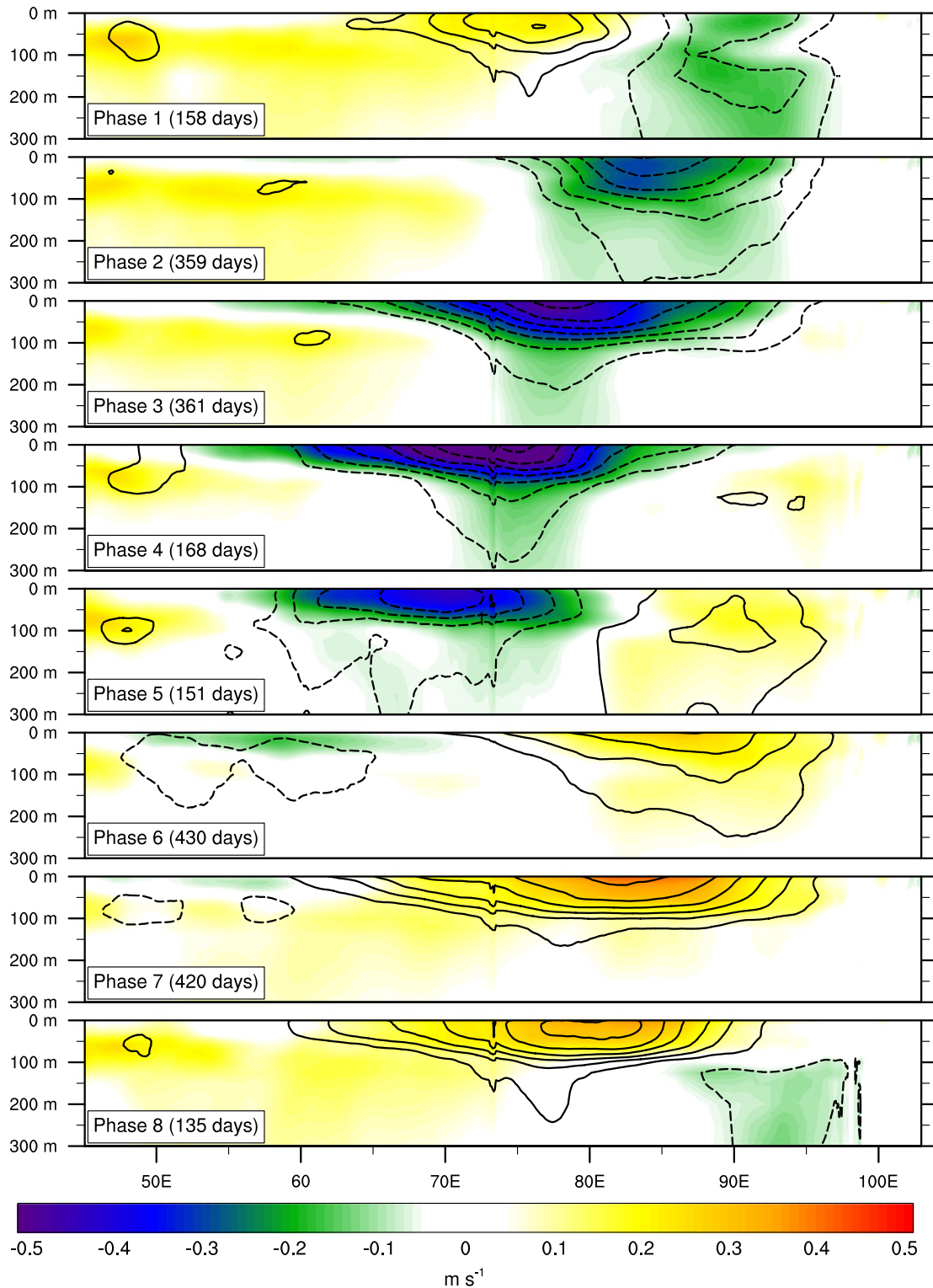


Figure 11. Composite of unfiltered zonal currents (shading, m s^{-1}) and 30–150-day band-pass-filtered zonal current anomalies (contours, m s^{-1}) based on the equatorial Rossby wave index are shown for phases 1–8. Data from 1994 to 2015 are shown. Zonal currents are averaged from 2°S to 2°N . Solid (negative) contours are positive (dashed). The contour interval is 0.05 m s^{-1} and omits the zero contour line. The number of days in each phase composite is shown in the bottom left.

shown that intraseasonal ER waves in the Indian Ocean result from a combination of these mechanisms where ER zonal accelerations in the ocean are generated directly by ISO wind stress as well as the reflection of energy at the eastern boundary (see also Figure 4). We expand on this work by examining the longitudinal variations of the forcing in greater detail, compositing wave features over a longer time period than previous observational studies, and comparing characteristics of currents for upwelling versus downwelling waves.

Figure 11 shows the zonal current anomalies averaged along the equator. This is based on the structure of equatorially symmetric Rossby waves, which have maximum SSH variability off the equator and maximum zonal velocity variability on the equator. The zonal current anomalies first appear in the subsurface of the eastern Indian Ocean during phase 8, indicating that the initiating mechanism for ER waves is not direct wind forcing which would manifest near the surface, but rather subsurface generation of wave momentum. The anomalous westward zonal current magnitude increases at the surface by phase 1, revealing a double minimum. An anomalous surface current minimum of -0.25 m s^{-1} rapidly develops at phase 2 near 85°E . The anomalous upper ocean westward currents are collocated with a minimum of the total westward current, indicating a strong relative contribution of intraseasonal currents to the total currents in the equatorial Indian Ocean, such that reversals of the intraseasonal current direction often coincide with a reversal of the total current direction. The anomalous zonal currents extend and propagate westward, with a maximum amplitude of 0.35 m s^{-1} in phases 3 and 4. The westward zonal current anomalies rapidly weaken to the west of 65°E , indicating that mechanisms of their maintenance are generally restricted to the eastern and central Indian Ocean. A similar pattern is observed for eastward currents; however, they weaken considerably to the west of 75°E . This demonstrates that westward currents propagate farther and with greater intensity than their eastward counterparts, similar to positive SSH anomalies (see Figure 3).

To illuminate the processes responsible for the development and maintenance of ER wave zonal currents along the equator, the zonal momentum budget is investigated using a combination of HYCOM ocean and ERA5 atmosphere reanalyses. The terms of the mixed layer average zonal momentum budget are calculated using the following equation:

$$\underbrace{\left(\frac{\partial u_{\text{ML}}}{\partial t}\right)'}_1 = \underbrace{\left(U_{\text{ML}} \cdot \nabla u_{\text{ML}}\right)'}_2 - \underbrace{\left(\frac{1}{\rho_{\text{ocean}}} \frac{\partial p_{\text{ML}}}{\partial x}\right)'}_3 + \underbrace{\left(\frac{u_{\text{air}} |u_{\text{air}}| C_d \rho_{\text{air}}}{\text{MLD} \times \rho_{\text{ocean}}}\right)'}_4 - \underbrace{\left(\frac{A_V}{\text{MLD}} \frac{\partial u}{\partial z}\right)'}_5 + \underbrace{A_H \nabla^2 u_{\text{ML}}}_6 \quad (5)$$

where U_{ML} is the horizontal ocean current averaged over the mixed layer, MLD is the mixed layer depth, u_{air} is the zonal wind, C_d is the wind-drag coefficient (0.0012), ρ_{air} is the air density (1.2 kg m^{-3}), ρ_{ocean} is the ocean density ($1,027 \text{ kg m}^{-3}$), and p is the ocean pressure. Term 1 is the acceleration of intraseasonal zonal current anomalies, term 2 is the horizontal advection of the zonal current anomalies, term 3 is the pressure gradient, term 4 is the anomalous wind stress, term 5 is the anomalous zonal shear stress at the base of the mixed layer, and term 6 is horizontal mixing. The pressure gradient acceleration is calculated as the residual of all other terms. The budget is evaluated from 2°S to 2°N , where contributions from Coriolis accelerations are small.

The negative zonal momentum tendency (i.e., westward acceleration) has two main features: (a) a local minimum that propagates from the eastern to western Indian Ocean and (b) a quasi-stationary local minimum across the Indian Ocean during phase 8 (Figure 12a). The zonal momentum tendency is a minimum ($-0.3 \text{ m s}^{-1} \text{ week}^{-1}$) where these two features overlap in the eastern Indian Ocean near 84°E during phase 1. Horizontal advection weakens westward currents in the eastern and parts of the central Indian Ocean at rates up to $+0.1 \text{ m s}^{-1} \text{ week}^{-1}$ (Figure 12b). The phase alignment of horizontal advection and westward currents shifts to the west of the Maldives (73°E), where horizontal advection modestly amplifies and propagates current magnitudes. This phase shift is perhaps related to the excitation of short Rossby waves by strong equatorial currents at the Maldives (Nagura & Masumoto, 2015). The analysis of horizontal advection indicates that ocean dynamics assist the acceleration of anomalous westward currents along the equator in parts of the central and much of the western Indian Ocean.

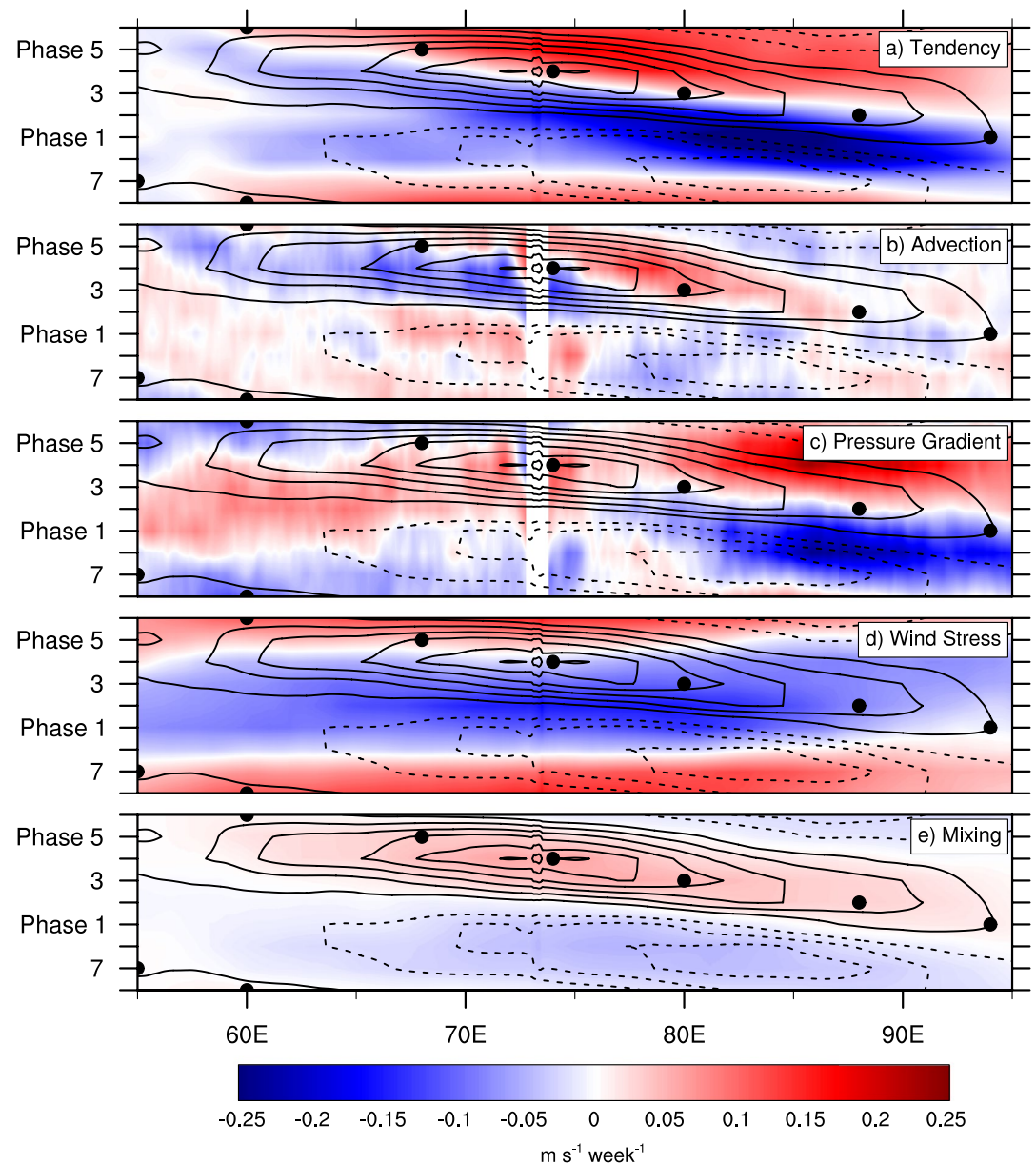


Figure 12. Composite of 30–150-day bandpass-filtered zonal current anomaly tendency terms (shading, m s^{-1}) and 30–150-day band-pass-filtered zonal current anomalies (contours, m s^{-1}) based on the equatorial Rossby wave index are shown for phases 1–8. Data from 1994 to 2015 are shown. The anomalous zonal current (a) tendency, (b) horizontal advection, (c) pressure gradient, (d) wind stress, and (e) shear stress and horizontal mixing are included. Zonal currents are averaged from 2°S to 2°N . Solid (dashed) contours are westward (eastward) currents. The contour interval is 0.1 m s^{-1} and omits the zero contour line. Black dots indicate approximate location of downwelling equatorial Rossby wave center.

The zonal current tendency owing to the pressure gradient is shown in Figure 12c. This term is strongest in the eastern Indian Ocean and is largely responsible for the propagation of westward currents to the west with a minimum of $-0.23 \text{ m s}^{-1} \text{ week}^{-1}$ at phase 8 and 87°E . Over most of the eastern Indian Ocean, the pressure gradient minimum is predominantly located ~ 2 phases ($1/4$ cycle) ahead of the anomalous current minima indicating a primary role in propagating the currents westward. Interestingly it only weakly contributes to the generation of currents in the far eastern Indian Ocean. The exception to this pattern is near and just to the west of the Maldives where the pressure gradient opposes the

tendency by horizontal advection (see Figure 12b) and the terms largely cancel. In the western Indian Ocean, the pressure gradient term is much weaker but generally weakens currents and slows the westward propagation.

The pressure gradient term is interpreted in the context of ISO wind stress that shifts ocean mass to the east, likely in the form of Kelvin waves (e.g., Pujiana & McPhaden, 2020). The pressure gradient forcing is a direct response to the eastward wind stress forcing, mass accumulation in the eastern Indian Ocean, and relative increase of high pressure along the coast of Sumatra. As a result, local eastward currents decelerate as westward currents accelerate. Although Kelvin waves are not expressly examined in this analysis of the momentum budget due to the narrow focus of the ER wave index utilized for formulating composites, they are critical to the initiation of ER waves in the eastern Indian Ocean as demonstrated in many previous studies of intraseasonal wind stress.

The acceleration of zonal current anomalies due to wind stress forcing is shown in Figure 12d. The wind stress displays a rapid propagation to the east, as might be expected given the previously shown relationship between ER waves and the ISO (see Figures 4 and 5). In the eastern Indian Ocean, wind stress forcing of $-0.05 \text{ m s}^{-1} \text{ week}^{-1}$ is largely in phase with westward zonal current anomalies, resulting in their amplification. In the central Indian Ocean, wind stress forcing of $-0.15 \text{ m s}^{-1} \text{ week}^{-1}$ predominantly leads westward currents by 2 phases and, as a result, propagates westward currents to the west while also slightly strengthening them. In the western Indian Ocean, westward wind stress of -0.05 to $-0.1 \text{ m s}^{-1} \text{ week}^{-1}$ continues to propagate the currents. This analysis shows that westward wind stress anomalies associated with the ISO generate, amplify, and propagate westward current anomalies across the equatorial Indian Ocean. Although the ER wave index is ill-posed to resolve eastward propagating Kelvin waves in the ocean, the generation of westward currents begins shortly after the terminus of the westerly wind stress in the Indian Ocean. Such westerly wind stress is known to drive ocean Kelvin waves that reflect as ER waves, and this reflection likely manifests as a reversal of the pressure gradient term discussed earlier.

The zonal shear stress at the base of the mixed layer as well as horizontal mixing combine to weaken zonal current anomalies regardless of the current direction (Figure 12e). The zonal shear stress is much stronger than the horizontal mixing. The shear stress increases as the westward zonal current increases with a maximum of $0.05 \text{ m s}^{-1} \text{ week}^{-1}$ at Phase 4 near 74°E , indicating that this sink of zonal momentum is proportional to the zonal current magnitude within the mixed layer.

5. Summary

Rydbeck, Jensen, Smith, et al. (2019) observed that intraseasonal OHC anomalies are maximized during periods of enhanced ISO convection in the central and western tropical Indian Ocean. They also observed that the majority of intraseasonal OHC variance is off-equatorial and westward propagating and hypothesized that westward propagating ER waves are responsible for the phase alignment of intraseasonal OHC and convection anomalies. The present study demonstrates the harmonization between intraseasonal modes in the atmosphere and ocean as well as the mechanisms of their synchronized symbiosis.

In order to identify the leading mode of westward propagating intraseasonal variability in the ocean and investigate its behavior, an index based on EOFs of AVISO SSH anomalies is developed. The EOF analysis reveals a mode with a zonal wavelength, phase speed, and frequency that agrees with the first baroclinic mode ER wave. The first two EOFs describe 41% of the westward propagating intraseasonal variance in the equatorial Indian Ocean. Composites of ocean and atmospheric variables based on the ER wave index show that waves are most intense in the eastern and central Indian Ocean and weaken in the western Indian Ocean.

The generation of downwelling ER waves in the eastern Indian Ocean is preceded by significant atmospheric intraseasonal variability characterized by strong westerly wind stress and enhanced convection known to generate downwelling Kelvin waves in the ocean. This atmospheric forcing is consistent with the behavior of the ISO and generates a reversal of the anomalous upper ocean pressure gradient in the eastern Indian Ocean. As the prevailing wind direction switches to westward in association with the suppressed convective phase of the ISO, ER wave currents are accelerated in the eastern Indian Ocean by the westward wind stress

Intraseasonal Oscillation and Rossby Wave Feedback Loop

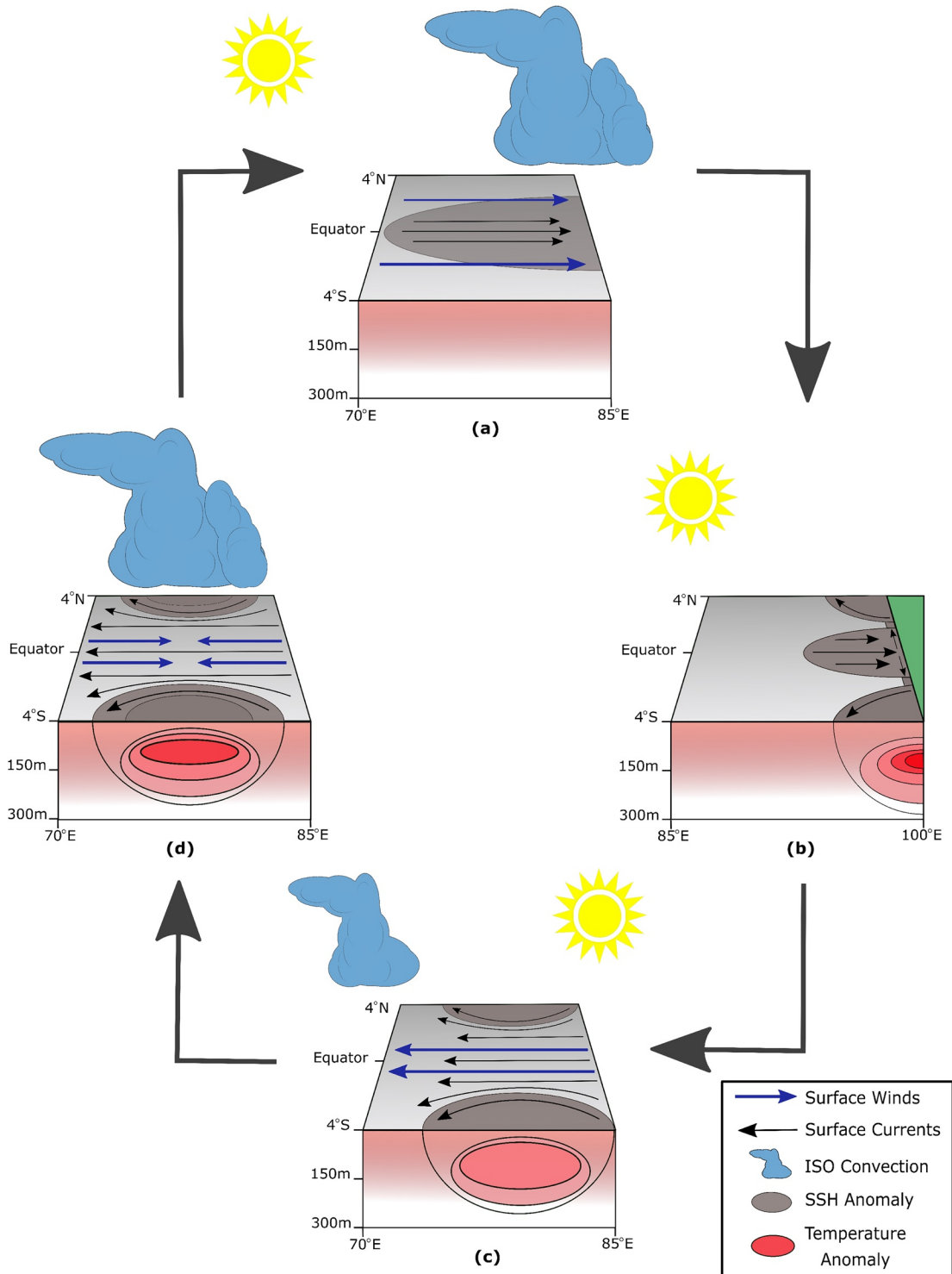


Figure 13.

and propagated westward by the pressure gradient forcing. The zonal currents maximize in the central Indian Ocean where the easterly wind stress acceleration ends.

ER waves generated by the wind stress significantly modulate the ocean environment through which they propagate. Positive OHC anomalies are in phase with downwelling waves, and the maximum OHC occurs in the central Indian Ocean 1 phase (~11 days) prior to the maximum of atmospheric convection anomalies at the same longitude. This suggests a positive ocean-atmosphere feedback. The intraseasonal budget of OHC reveals that these positive OHC anomalies develop in response to ocean dynamical forcing, particularly vertical and meridional advection, with a secondary role by atmospheric flux forcing. Thus, OHC anomalies are not simply a consequence of contemporaneous atmospheric forcing, but have leading contributions from ocean planetary wave dynamics that lag the initial ISO forcing by ~45 days.

Correctly representing the interactions between the ISO and oceanic planetary waves has important implications for accurate subseasonal predictions (e.g., Gadgil et al., 2019). Coupled models that poorly represent the ISO and related intraseasonal wind stress variations in the tropical Indian Ocean are also likely to underestimate the amplitude of first baroclinic mode ER waves and related intraseasonal OHC variability. Such models are also likely to underrepresent the oceanic intraseasonal pathway whereby successive eastward propagating ISO events are able to communicate in the form of westward propagating oceanic ER waves.

A summary of the synchronized behavior responsible for the coevolution of ER waves and the ISO is shown in Figure 13 (see also Figure 9 of Webber, Matthews, et al., 2012). In Figure 13a, westerly surface wind stress anomalies generated by the ISO accumulate mass in the eastern Indian Ocean generating a westward oriented pressure gradient. This is quickly followed by periods of easterly wind stress anomalies. In response to these two forcing mechanisms, first baroclinic mode downwelling ER waves develop and subsequently propagate westward (Figures 13b and 13c). The waves are amplified by westward wind stress anomalies positioned ahead of the next enhanced convective phase of the ISO (Figure 13c). The downwelling ER waves depress the isotherms and increases the OHC in the central Indian Ocean. When the westward propagating ER waves and the eastward propagating ISO cross paths, ISO convection intensifies in association with the positive OHC anomalies (Figure 13d). In this framework, ER waves are generated and subsequently strengthened by oppositely signed ISO wind stress forcing. They are hypothesized to positively feedback onto the ISO by enhancing atmospheric convection and strengthening the diabatically forced atmospheric wind response from which the waves are generated and amplified.

Similarly synchronous patterns between intraseasonal convection and OHC are observed when composite averaging is based on an atmospheric index of ISO variability (Rydbeck, Jensen, Smith, et al., 2019), indicating that the positive feedback loop between ER waves and the ISO is not particularly sensitive to the choice of intraseasonal “lens” through which it is viewed. The primary harmonization mechanisms between these atmosphere and ocean intraseasonal modes are wind stress and OHC. The manner in which OHC anomalies modulate the SST, surface latent and sensible heat fluxes, and, ultimately, atmospheric convection is very much an open research question. We speculate that the anomalous increase of OHC during the enhanced convective phase of the ISO retards the rate of sea surface cooling generated by atmospheric heat flux forcing and mixing. The net effect of OHC variations on SST during ISO events is the subject of future fully coupled modeling work.

Figure 13. Schematic showing the temporal evolution of equatorial Rossby (ER) waves and intraseasonal oscillation convection in the tropical Indian Ocean. Panel (a) shows the generation of the equatorial Kelvin wave associated with anomalous westerly winds at and behind the convective envelope. Panel (b) shows the reflection of the Kelvin wave into ER waves. Panel (c) shows the westward propagation of the ER waves and development of easterly wind stress in advance of the intraseasonal oscillation convection. Panel (d) shows the resulting strengthening of ER waves and the intensification of intraseasonal convection over the region of increased OHC. The vertical cross section shows the temperature anomalies at 4°S.

Data Availability Statement

Data analyzed in this study are a reanalysis of existing and publicly available data. AVISO SSH data (Pascual et al., 2006) and ERA5 winds (Hersbach et al., 2020) are available at <https://marine.copernicus.eu/>. NOAA SST data (Reynolds et al., 2007) are available at <https://psl.noaa.gov/>. NOAA OLR (Lee, 2011) data are available at <https://www.ncdc.noaa.gov/>. OSCAR surface current data (Bonjean & Lagerloef, 2002; ESR, 2009) are available at <https://podaac.jpl.nasa.gov/>. HYCOM reanalysis data (Metzger et al., 2017) are available at <https://www.hycom.org/>. Surface forcing field data from the NCEP CFSR (Saha et al., 2010) are available at <https://www.ncdc.noaa.gov/>.

Acknowledgments

The authors thank five anonymous reviewers for providing comments and suggestions that greatly benefited this manuscript. This research is supported by the Office of Naval Research Department Research Initiatives MISO-BoB & PISTON and the US Naval Research Laboratory's 6.1 base program project, IRCSOME.

References

- Adames, Á. F., & Wallace, J. M. (2015). Three-dimensional structure and evolution of the moisture field in the MJO. *Journal of the Atmospheric Sciences*, 72(10), 3733–3754. <https://doi.org/10.1175/JAS-D-15-0003.1>
- Azaneu, M. V. C., Matthews, A. J., & Baranowski, D. B. (2021). Subsurface oceanic structure associated with atmospheric convectively coupled equatorial Kelvin waves in the eastern Indian Ocean. *Journal of Geophysical Research: Oceans*, 126(7), e2021JC017171. <https://doi.org/10.1029/2021jc017171>
- Bonjean, F., & Lagerloef, G. S. E. (2002). Diagnostic model and analysis of the surface currents in the tropical Pacific Ocean. *Journal of Physical Oceanography*, 32(10), 2938–2954. [https://doi.org/10.1175/1520-0485\(2002\)032<2938:DMAAOT>2.0.CO;2](https://doi.org/10.1175/1520-0485(2002)032<2938:DMAAOT>2.0.CO;2)
- Chowdary, J. S., Gnanaseelan, C., & Xie, S. P. (2009). Westward propagation of barrier layer formation in the 2006–07 Rossby wave event over the tropical southwest Indian Ocean. *Geophysical Research Letters*, 36(4), L04607. <https://doi.org/10.1029/2008GL036642>
- Del Genio, A. D., & Chen, Y. (2015). Cloud-radiative driving of the Madden-Julian oscillation as seen by the A-Train. *Journal of Geophysical Research: Atmospheres*, 120(11), 5344–5356. <https://doi.org/10.1002/2015JD023278>
- DeMott, C. A., Klingaman, N. P., & Woolnough, S. J. (2015). Atmosphere-ocean coupled processes in the Madden-Julian oscillation. *Reviews of Geophysics*, 53, 1099–1154. <https://doi.org/10.1002/2014RG000478>
- Effy, J. B., Francis, P. A., Ramakrishna, S. S. V. S., & Mukherjee, A. (2020). Anomalous warming of the western equatorial Indian Ocean in 2007: Role of ocean dynamics. *Ocean Modelling*, 147, 101542. <https://doi.org/10.1016/j.ocemod.2019.101542>
- Emanuel, K. A. (1987). An air-sea interaction model of intraseasonal oscillations in the tropics. *Journal of the Atmospheric Sciences*, 44(16), 2324–2340. [https://doi.org/10.1175/1520-0469\(1987\)044<2324:aasimo>2.0.co;2](https://doi.org/10.1175/1520-0469(1987)044<2324:aasimo>2.0.co;2)
- ESR. (2009). OSCAR third degree resolution ocean surface currents. <https://doi.org/10.5067/OSCAR-03D01>
- Fu, L. L. (2007). Intraseasonal variability of the equatorial Indian Ocean observed from sea surface height, wind, and temperature data. *Journal of Physical Oceanography*, 37(2), 188–202. <https://doi.org/10.1175/JPO3006.1>
- Gadgil, S., Francis, P. A., & Vinayachandran, P. N. (2019). Summer monsoon of 2019: Understanding the performance so far and speculating about the rest of the season. *Current Science*, 117(5), 783–793. <https://doi.org/10.18520/cs/v117/5/783-793>
- Halkides, D. J., Waliser, D. E., Lee, T., Menemenlis, D., & Guan, B. (2015). Quantifying the processes controlling intraseasonal mixed-layer temperature variability in the tropical Indian Ocean. *Journal of Geophysical Research: Oceans*, 120(2), 692–715. <https://doi.org/10.1002/2014JC010139>
- Han, W. (2005). Origins and dynamics of the 90-day and 30–60-day variations in the equatorial Indian Ocean. *Journal of Physical Oceanography*, 35(5), 708–728. <https://doi.org/10.1175/JPO2725.1>
- Han, W., Lawrence, D. M., & Webster, P. J. (2001). Dynamical response of equatorial Indian Ocean to intraseasonal winds: Zonal flow. *Geophysical Research Letters*, 28(22), 4215–4218. <https://doi.org/10.1029/2001GL013701>
- Han, W., McCreary, J. P., Anderson, D. L. T., & Mariano, A. J. (1999). Dynamics of the eastern surface jets in the equatorial Indian Ocean. *Journal of Physical Oceanography*, 29(9), 2191–2209. [https://doi.org/10.1175/1520-0485\(1999\)029<2191:DOTESJ>2.0.CO;2](https://doi.org/10.1175/1520-0485(1999)029<2191:DOTESJ>2.0.CO;2)
- Han, W., McCreary, J. P., Masumoto, Y., Vialard, J., & Duncan, B. (2011). Basin resonances in the equatorial Indian Ocean. *Journal of Physical Oceanography*, 41(6), 1252–1270. <https://doi.org/10.1175/2011JPO4591.1>
- Henderson, S. A., Maloney, E. D., & Barnes, E. A. (2016). The influence of the Madden-Julian oscillation on Northern Hemisphere winter blocking. *Journal of Climate*, 29(12), 4597–4616. <https://doi.org/10.1175/JCLI-D-15-0502.1>
- Hersbach, H., Bell, B., Berrisford, P., Hirahara, S., Horányi, A., Muñoz-Sabater, J., et al. (2020). The ERA5 global reanalysis. *Quarterly Journal of the Royal Meteorological Society*, 146, 1999–2049. <https://doi.org/10.1002/qj.3803>
- Hsu, P. C., & Li, T. (2012). Role of the boundary layer moisture asymmetry in causing the eastward propagation of the Madden-Julian oscillation. *Journal of Climate*, 25(14), 4914–4931. <https://doi.org/10.1175/JCLI-D-11-00310.1>
- Iskandar, I., Mardiansyah, W., Masumoto, Y., & Yamagata, T. (2005). Intraseasonal Kelvin waves along the southern coast of Sumatra and Java. *Journal of Geophysical Research*, 110(4). <https://doi.org/10.1029/2004JC002508>
- Iskandar, I., & McPhaden, M. J. (2011). Dynamics of wind-forced intraseasonal zonal current variations in the equatorial Indian Ocean. *Journal of Geophysical Research*, 116(6), C06019. <https://doi.org/10.1029/2010JC006864>
- Jensen, T. G. (1993). Equatorial variability and resonance in a wind-driven Indian Ocean model. *Journal of Geophysical Research*, 98(C12), 22533–22552. <https://doi.org/10.1029/93JC02565>
- Jensen, T. G., Shinoda, T., Chen, S., & Flatau, M. (2015). Ocean response to CINDY/DYNAMO MJOs in air-sea-coupled COAMPS. *Journal of the Meteorological Society of Japan. Series II*, 93A, 157–178. <https://doi.org/10.2151/jmsj.2015-049>
- Kikuchi, K., Wang, B., & Kajikawa, Y. (2012). Bimodal representation of the tropical intraseasonal oscillation. *Climate Dynamics*, 38(9–10), 1989–2000. <https://doi.org/10.1007/s00382-011-1159-1>
- Kiladis, G. N., Dias, J., Straub, K. H., Wheeler, M. C., Tulich, S. N., Kikuchi, K., et al. (2014). A comparison of OLR and circulation-based indices for tracking the MJO. *Monthly Weather Review*, 142(5), 1697–1715. <https://doi.org/10.1175/MWR-D-13-00301.1>
- Knutson, T., & Weickmann, K. (1987). 30–60 day atmospheric oscillations: Composite life cycles of convection and circulation anomalies. *Monthly Weather Review*, 115(7), 1407–1436. [https://doi.org/10.1175/1520-0493\(1987\)115<1407:daoclc>2.0.co;2](https://doi.org/10.1175/1520-0493(1987)115<1407:daoclc>2.0.co;2)
- Lau, K.-M., & Peng, L. (1987). Origin of low-frequency (intraseasonal) oscillations in the tropical atmosphere. Part I: Basic theory. *Journal of the Atmospheric Sciences*, 44(6), 950–972. [https://doi.org/10.1175/1520-0469\(1987\)044<0950:oofoi>2.0.co;2](https://doi.org/10.1175/1520-0469(1987)044<0950:oofoi>2.0.co;2)

- Lee, H.-T. (2011). NOAA climate data record (CDR) of daily outgoing longwave radiation (OLR), version 1.2. <https://doi.org/10.7289/VSSJ1HH2>
- Madden, R. A., & Julian, P. R. (1971). Detection of a 40–50 day oscillation in the zonal wind in the tropical Pacific. *Journal of the Atmospheric Sciences*, 28(5), 702–708. [https://doi.org/10.1175/1520-0469\(1971\)028<0702:DOADOI>2.0.CO;2](https://doi.org/10.1175/1520-0469(1971)028<0702:DOADOI>2.0.CO;2)
- Matthews, A. J. (2008). Primary and successive events in the Madden-Julian oscillation. *Quarterly Journal of the Royal Meteorological Society*, 134(631), 439–453. <https://doi.org/10.1002/qj.224>
- Metzger, E. J., Helber, R. W., Hogan, P. J., Posey, P. G., Thoppil, P. G., Townsend, T. L., et al. (2017). *Global ocean forecast system 3.1 validation testing*. (Technical Report). Naval Research Laboratory. Retrieved from <http://www.dtic.mil/docs/citations/AD1034517>
- Moum, J. N., Pujiana, K., Lien, R. C., & Smyth, W. D. (2016). Ocean feedback to pulses of the Madden-Julian oscillation in the equatorial Indian Ocean. *Nature Communications*, 7, 13203. <https://doi.org/10.1038/ncomms13203>
- Murtugudde, R., McCreary, J. P., & Busalacchi, A. J. (2000). Oceanic processes associated with anomalous events in the Indian Ocean with relevance to 1997–1998. *Journal of Geophysical Research*, 105, 3295–3306. <https://doi.org/10.1029/1999jc900294>
- Nagura, M., & Masumoto, Y. (2015). A wake due to the Maldives in the Eastward Wyrktii jet. *Journal of Physical Oceanography*, 45(7), 1858–1876. <https://doi.org/10.1175/JPO-D-14-0191.1>
- Nagura, M., & McPhaden, M. J. (2010). Dynamics of zonal current variations associated with the Indian Ocean dipole. *Journal of Geophysical Research*, 115(11), C11026. <https://doi.org/10.1029/2010JC006423>
- Nagura, M., & McPhaden, M. J. (2012). The dynamics of wind-driven intraseasonal variability in the equatorial Indian Ocean. *Journal of Geophysical Research*, 117(2). <https://doi.org/10.1029/2011JC007405>
- Neelin, J. D., Held, I. M., & Cook, K. H. (1987). Evaporation-wind feedback and low-frequency variability in the tropical atmosphere. *Journal of the Atmospheric Sciences*, 44(16), 2341–2348. [https://doi.org/10.1175/1520-0469\(1987\)044<2341:EWFALF>2.0.CO;2](https://doi.org/10.1175/1520-0469(1987)044<2341:EWFALF>2.0.CO;2)
- North, G. R., Bell, T. L., Cahalan, R. F., & Moeng, F. J. (1982). Sampling errors in the estimation of empirical orthogonal functions. *Monthly Weather Review*, 110(7), 699–706. [https://doi.org/10.1175/1520-0493\(1982\)110<0699:SEITEO>2.0.CO;2](https://doi.org/10.1175/1520-0493(1982)110<0699:SEITEO>2.0.CO;2)
- Pacanowski, R. C., & Griffies, S. (2000). *MOM 3.0 manual*. Retrieved from http://www.mom-ocean.science/web/docs/project/MOM3_manual.pdf
- Pascual, A., Faugère, Y., Larnicol, G., & Le Traon, P. Y. (2006). Improved description of the ocean mesoscale variability by combining four satellite altimeters. *Geophysical Research Letters*, 33(2), L02611. <https://doi.org/10.1029/2005GL024633>
- Pujiana, K., & McPhaden, M. J. (2020). Intraseasonal Kelvin waves in the equatorial Indian Ocean and their propagation into the Indonesian seas. *Journal of Geophysical Research: Oceans*, 125(5). <https://doi.org/10.1029/2019jc015839>
- Raymond, D. (2001). A new model of the Madden-Julian oscillation. *Journal of the Atmospheric Sciences*, 58(18), 2807–2819. [https://doi.org/10.1175/1520-0469\(2001\)058<2807:anmotm>2.0.co;2](https://doi.org/10.1175/1520-0469(2001)058<2807:anmotm>2.0.co;2)
- Reynolds, R. W., Smith, T. M., Liu, C., Chelton, D. B., Casey, K. S., & Schlax, M. G. (2007). Daily high-resolution-blended analyses for sea surface temperature. *Journal of Climate*, 20(22), 5473–5496. <https://doi.org/10.1175/2007JCLI1824.1>
- Roundy, P. E. (2020). Interpretation of the spectrum of eastward-moving tropical convective anomalies. *Quarterly Journal of the Royal Meteorological Society*, 146(727), 795–806. <https://doi.org/10.1002/qj.3709>
- Ruppert, J. H., & Johnson, R. H. (2015). Diurnally modulated cumulus moistening in the preonset stage of the Madden-Julian oscillation during DYNAMO. *Journal of the Atmospheric Sciences*, 72(4), 1622–1647. <https://doi.org/10.1175/JAS-D-14-0218.1>
- Rydbeck, A. V., & Jensen, T. G. (2017). Oceanic impetus for convective onset of the Madden-Julian oscillation in the western Indian Ocean. *Journal of Climate*, 30(11), 4299–4316. <https://doi.org/10.1175/JCLI-D-16-0595.1>
- Rydbeck, A. V., Jensen, T. G., & Flatau, M. (2019). Characterization of intraseasonal Kelvin waves in the equatorial Pacific Ocean. *Journal of Geophysical Research: Oceans*, 124(3), 2028–2053. <https://doi.org/10.1029/2018JC014838>
- Rydbeck, A. V., Jensen, T. G., & Igel, M. R. (2019). Idealized modeling of the atmospheric boundary layer response to SST forcing in the Western Indian Ocean. *Journal of the Atmospheric Sciences*, 76(7), 2023–2042. <https://doi.org/10.1175/JAS-D-18-0303.1>
- Rydbeck, A. V., Jensen, T. G., & Nyadjro, E. S. (2017). Intraseasonal sea surface warming in the western Indian Ocean by oceanic equatorial Rossby waves. *Geophysical Research Letters*, 44(9), 4224–4232. <https://doi.org/10.1002/2017GL073331>
- Rydbeck, A. V., Jensen, T. G., Smith, T. A., Flatau, M. K., Janiga, M. A., Reynolds, C. A., & Ridout, J. A. (2019). Ocean heat content and the intraseasonal oscillation. *Geophysical Research Letters*, 46, 14558–14566. <https://doi.org/10.1029/2019GL084974>
- Saha, S., Moorthi, S., Pan, H. L., Wu, X., Wang, J., Nadiga, S., et al. (2010). The NCEP climate forecast system reanalysis. *Bulletin of the American Meteorological Society*, 91(8), 1015–1058. <https://doi.org/10.1175/2010BAMS3001.1>
- Sengupta, D., Senan, R., Goswami, B. N., & Vialard, J. (2007). Intraseasonal variability of equatorial Indian Ocean zonal currents. *Journal of Climate*, 20(13), 3036–3055. <https://doi.org/10.1175/JCLI4166.1>
- Shinoda, T., Jensen, T. G., Flatau, M., Chen, S., Han, W., & Wang, C. (2013). Large-scale oceanic variability associated with the Madden-Julian oscillation during the CINDY/DYNAMO field campaign from satellite observations. *Remote Sensing*, 5(5), 2072–2092. <https://doi.org/10.3390/rs5052072>
- Straub, K. H., & Kiladis, G. N. (2002). Observations of a convectively coupled Kelvin wave in the eastern Pacific ITCZ. *Journal of the Atmospheric Sciences*, 59(1), 30–53. [https://doi.org/10.1175/1520-0469\(2002\)059<0030:OOACCK>2.0.CO;2](https://doi.org/10.1175/1520-0469(2002)059<0030:OOACCK>2.0.CO;2)
- Vialard, J., Shenoi, S. S. C., McCreary, J. P., Shankar, D., Durand, F., Fernando, V., & Shetye, S. R. (2009). Intraseasonal response of the northern Indian Ocean coastal waveguide to the Madden-Julian oscillation. *Geophysical Research Letters*, 36(14), L14606. <https://doi.org/10.1029/2009GL038450>
- Vinayachandran, P. N., Francis, P. A., & Rao, S. A. (2009). Indian Ocean dipole: Processes and impacts. In *Current trends in science* (pp. 569–589). Retrieved from <http://moeseprints.incois.gov.in/97/>
- Vinayachandran, P. N., Iizuka, S., & Yamagata, T. (2002). Indian Ocean dipole mode events in an ocean general circulation model. *Deep-Sea Research Part II: Topical Studies in Oceanography*, 49(7–8), 1573–1596. [https://doi.org/10.1016/S0967-0645\(01\)00157-6](https://doi.org/10.1016/S0967-0645(01)00157-6)
- Vinayachandran, P. N., Saji, N. H., & Yamagata, T. (1999). Response of the equatorial Indian Ocean to an unusual wind event during 1994. *Geophysical Research Letters*, 26(11), 1613–1616. <https://doi.org/10.1029/1999GL900179>
- Wang, B., Chen, G., & Liu, F. (2019). Diversity of the Madden-Julian oscillation. *Science Advances*, 5(7), eaax0220. <https://doi.org/10.1126/sciadv.aax0220>
- Webber, B. G. M., Matthews, A. J., & Heywood, K. J. (2010). A dynamical ocean feedback mechanism for the Madden-Julian oscillation. *Quarterly Journal of the Royal Meteorological Society*, 136(648), 740–754. <https://doi.org/10.1002/qj.604>
- Webber, B. G. M., Matthews, A. J., Heywood, K. J., & Stevens, D. P. (2012). Ocean Rossby waves as a triggering mechanism for primary Madden-Julian events. *Quarterly Journal of the Royal Meteorological Society*, 138(663), 514–527. <https://doi.org/10.1002/qj.936>
- Webber, B. G. M., Stevens, D. P., Matthews, A. J., & Heywood, K. J. (2012). Dynamical ocean forcing of the Madden-Julian oscillation at lead times of up to five months. *Journal of Climate*, 25(8), 2824–2842. <https://doi.org/10.1175/JCLI-D-11-00268.1>

- Weickmann, K. M., Lussy, G. R., & Kutzbach, J. E. (1985). Intraseasonal (30-60 day) fluctuations of outgoing longwave radiation and 250 mb streamfunction during northern winter. *Monthly Weather Review*, *113*(6), 941–961. [https://doi.org/10.1175/1520-0493\(1985\)113<0941:IDFOOL>2.0.CO;2](https://doi.org/10.1175/1520-0493(1985)113<0941:IDFOOL>2.0.CO;2)
- West, B. J., Han, W., & Li, Y. (2018). The role of oceanic processes in the initiation of Indian summer monsoon intraseasonal oscillations over the Indian Ocean. *Journal of Geophysical Research: Oceans*, *123*(5), 3685–3704. <https://doi.org/10.1029/2017JC013564>
- West, B. J., Han, W., Zhang, L., & Li, Y. (2020). The role of oceanic processes in the initiation of boreal winter intraseasonal oscillations over the Indian Ocean. *Journal of Geophysical Research: Oceans*, *125*(2), e2019JC015426. <https://doi.org/10.1029/2019JC015426>
- Wheeler, M. C., & Hendon, H. H. (2004). An all-season real-time multivariate MJO index: Development of an index for monitoring and prediction. *Monthly Weather Review*, *132*(8), 1917–1932. [https://doi.org/10.1175/1520-0493\(2004\)132<1917:AARMMI>2.0.CO;2](https://doi.org/10.1175/1520-0493(2004)132<1917:AARMMI>2.0.CO;2)
- Wheeler, M. C., & Kiladis, G. N. (1999). Convectively coupled equatorial waves: Analysis of clouds and temperature in the wavenumber-frequency domain. *Journal of the Atmospheric Sciences*, *56*(3), 374–399. [https://doi.org/10.1175/1520-0469\(1999\)056<0374:CCEWAO>2.0.CO;2](https://doi.org/10.1175/1520-0469(1999)056<0374:CCEWAO>2.0.CO;2)